Additive Manufacturing in Aerospace: Influence of surface conditions on the fatigue life of Ti-6Al-4V produced by laser powder bed fusion

Master Thesis

Alegre Ituarte, Javier (javal678)

Supervisor: Magnus Kahlin

Examiner: Johan Moverare

Linköpings universitet
Department of Management and Engineering (IEI)
The Division of Engineering Materials
Spring 2024 — ISRN-LIU-IEI-TEK-A–24/04796–SE

Abstract

This thesis investigates the influence of surface conditions on the fatigue life of Ti-6Al-4V components produced by laser powder bed fusion (L-PBF) for aerospace applications. It is a part of a two ongoing research projects at the Department of Management and Engineering (IEI) coordinated by Saab Aeronautics. The project is financed by Vinnova via the NFFP and Innovair programs. The advantages of additive manufacturing technologies specifically L-PBF has enabled the creation of complex geometries and lightweight structures that makes it suitable for the weight-critical application like Aerospace. This study focuses on Ti-6Al-4V,that is known for its high strength-to-weight ratio, corrosion resistance, and suitability for high-temperature applications. The research objectives include characterizing surface roughness, understanding its interaction with geometrical stress concentrations, the characterisation of the fatigue initiation points and evaluating the fatigue behavior of both as-built and Hirtisation-treated specimens under constant and variable amplitude loading. This thesis will focus on surface roughness measurements, tensile testing, and fatigue testing. Advanced characterization techniques, including stereo-microscopy and scanning electron microscopy, are employed to analyze fracture surfaces and crack initiation points. The results indicate that the effect of surface roughness of the specimens that has the same Kt on fatigue life is not strong enough. The findings contribute to a deeper understanding of fatigue behavior in AM Ti-6Al-4V parts and highlight the importance of surface treatment in optimizing the fatigue life of aerospace components. This research provides more insights for the development and application of AM in high fatigue load application in the aerospace industry.

Nomenclature

AM	additive manufacturing
AB	as-built
B.d.	build direction
Hirt.	hirtisation
CA	constant amplitude
VA	variable amplitude
CAD	computer aided design
FALSTAFF	fighter aircraft loading standard for fatigue
FCG	fatigue crack growth
HIP	hot isostatic pressing
LOF	lack of fusion
L-PBF	laser power bed fusion
SR	surface roughness
SEM	scanning electron microscope
RFC	rainflow counting

Contents

1 Introduction

Additive manufacturing (AM) or 3D printing technologies, such as laser powder bed fusion (L-PBF), have been discovered as a possible method for producing complex and lightweight part with topologically optimized geometries. These innovations have the ability to overcome the constraints of traditional subtractive methods, resulting in more efficient structures, reduced fuel consumption, and lower airplane emissions. However, when it comes to load-bearing structures in aviation, fatigue behavior is a critical design consideration as it directly impacts both economic lifespan and safety. While AM technology has been around for a while, understanding fatigue behavior in complex AM parts remains in its early stages. The inherent surface roughness and presence of internal defects in AM materials significantly influence their fatigue performance. Fortunately, post-processing techniques like hirtisation can offer improvements in fatigue strength. To fully leverage the advantages of AM, a deeper understanding of fatigue behavior in these materials is crucial. This Master's thesis, titled "Additive Manufacturing in Aerospace: Influence of surface conditions on the fatigue life of Ti-6Al-4V produced by L-PBF" aims to enhance our understanding of fatigue behavior in AM parts by investigating the influence of factors like surface roughness, internal defects, and geometry of the components. A key focus will be on gaining a deeper understanding of how surface condition affects the fatigue performance of Ti-6Al-4V samples produced using L-PBF.

1.1 Additive manufacturing

Additive Manufacturing has become increasingly popular because it allows for the creation of complex shapes without needing any further machining processes. Charles Hull was the trailblazer of this technology with his invention of stereo-lithography (SLA) back in 1986 [1]. This innovation kicked off a variety of other AM methods, such as powder bed fusion, fused deposition modeling, and inkjet printing. Initially embraced for its cost-effectiveness and swift production times, 3D printing quickly became a favorite for architects and designers to whip up prototypes in the early design phases. But it didn't stop there - metal AM soon took the manufacturing world by storm, shifting from just making prototypes to full-scale production [2]. What sets AM apart is how it builds final products straight from computer designs by stacking material layer upon layer, which is quite the opposite of the traditional way of making things by cutting away material. This layering technique opens up a whole new world of design possibilities, making it easier to craft complex forms that could either boost how well something works or cut down on how much it costs to make it. In the past, crafting aerospace parts was an exercise in precision chiseling and sculpting away material to form the final product through subtractive manufacturing. Then came 3D printing, turning the whole process upside down. Unlike the traditional methods that cut away, additive manufacturing builds up a product from a three-dimensional model, one layer at a time as shown in Figure 1. This technique has recently integrated onto the market as a powerhouse for production, opening doors to customized designs and increased production efficiency.

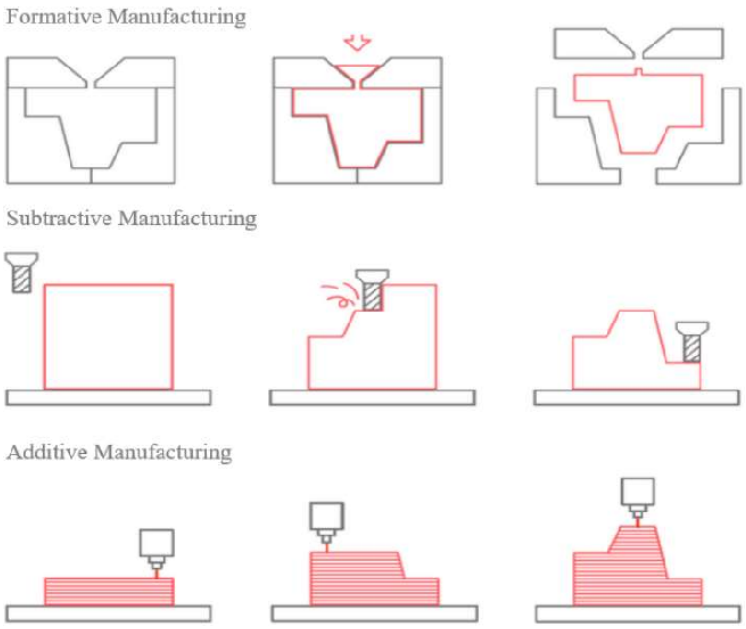

Figure 1: A picture describing the three manufacture methods from the "A hybrid additive and subtractive manufacturing approach for multi-material components " paper [3].

1.1.1 Processes

There are various AM processes capable of shaping metal parts. The American Society for Testing and Materials' International Committee has categorized these processes into seven main types: binder jetting, directed energy deposition (DED), material extrusion, material jetting, powder bed fusion (PBF), sheet lamination, and vat photo-polymerization [4]. In the aerospace world, these technologies split into two broad groups based on the material they use: one for metals and another for non-metals.For non-metallic parts, additive manufacturing uses different materials that includes plastics, ceramics, and even sand. The techniques that are used with these materials are stereo-lithography, multi-jet modeling, fused deposition modeling and freeze-form extrusion fabrication [5].

When it comes to metals, there are mainly DED and PBF methods. The DED techniques are laser metal deposition (LMD), laser engineering net shaping (LENS), electron beam welding (EBW), electron beam free-form fabrication (EBF3), and wire arc additive manufacturing (WAAM). Meanwhile, PBF is known for its specialized processes such as Direct Metal Laser Sintering (DMLS), Selective Laser Melting (SLM), and Electron Beam Melting (EBM) [6]. Beyond these, some applications also uses binder jetting and supersonic particle deposition (SPD), often referred to as cold spray.

In this thesis, our focus will be on PBF for creating parts from the titanium alloy Ti-6Al-4V. L-PBF (L-PBF) is working in a way like crafting art from metal dust using laser. As shown in Figure 2, a fine layer of titanium alloy powder spread across a bed, and then a laser, precise and controlled, moves over its surface. This laser isn't just moving randomly; it's following a detailed digital blueprint, melting

and fusing the powder into solid metal. With each pass, the bed lowers slightly, a new layer of powder is applied, and the laser is activated again, building up the part layer by layer from the ground up.

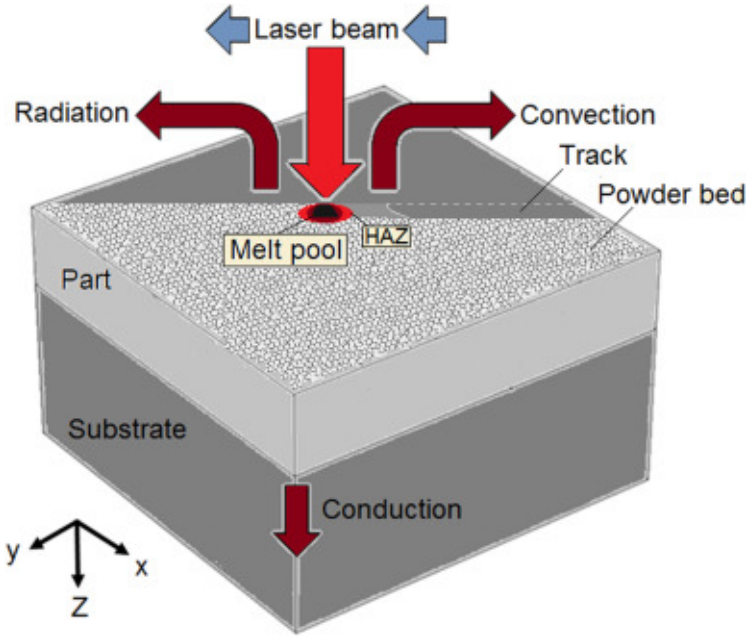

Figure 2: A picture describing typical L-PBF process consisting of a single moving laser beam, powder bed, solidified tracks, part and substrate; paper [7].

The process starts with a 2D drawing and 3D model of the parts as shown in section 4.2.1. This model is then sliced into thin horizontal layers, translating it into instructions for the laser. In the machine, a thin layer of Ti-6Al-4V powder is spread evenly over the build platform. The laser, guided by the model's slices, selectively melts the powder where the part needs to be built, solidifying the powder into a solid metal layer. Once a layer is complete, the build platform drops down the thickness of one layer, and a new layer of powder is spread on top. The laser then fuses this new layer to the previous one, building the part up from the bottom. But it's not just about melting metal. Another big advantage of L-PBF is its precision and control. The laser's parameters, like its power, speed, and focus, are finely tuned to ensure that the metal doesn't just melt, but does that in a way that produces strong, dense parts with the desired properties. The atmosphere inside the build chamber is another critical factor. After the part is fully built, it is still not ready to be used yet. It often requires post-processing, like heat treatments to relieve stresses or machining to achieve the final dimensions and surface finish [8].

1.1.2 Materials

A very important aspect in AM is the choice of material, which is not only based on the feasibility of manufacturing complex designs but also the performance and application of the required product. This chapter illustrates the spectrum of materials that are used in AM processes highlighting the applications that might use these materials, their properties, and the considerations involved in their selection. Polymers

are widely used in AM for their versatility, color options, and ease of processing. ABS (Acrylonitrile Butadiene Styrene) and PLA (Polylactic Acid) are common for prototypes and non-load-bearing components due to their excellent printability [9]. Another material that is characterized by its high temperature resistance, hardness, and electrical insulation properties is ceramics. Silicon carbide, zirconia, and alumina are used in AM for specialized applications like aerospace, automotive, and biomedical fields for components that require high wear resistance and thermal stability [10]. Despite these advantages, the production of ceramic parts via AM is challenging and that is due to the materials brittleness.
Aerospace applications also use composite materials in AM of different parts as a way to benefit from combining two or more distinct materials. Carbon fiber reinforced polymers (CFRP) are used for parts that require high stiffness and strength-to-weight ratio [11]. Glass fibers, metal powders, or other fillers are added to polymers to enhance mechanical properties, thermal resistance, and electrical conductivity. The ability to tailor the distribution and orientation of these fillers in AM processes opens new possibilities for functionally graded materials and parts with localized reinforcement.

Metals stand at the top of our focus in this master thesis and in the AM materials in general, due to their structural integrity and functionality. Stainless steels, offering corrosion resistance and high strength, are utilized in automotive and tooling applications. Inconel, a nickel-chromium-based super-alloy, is favored for its exceptional heat and corrosion resistance, ideal for turbine blades and high-temperature applications. Aluminum alloys, known for their lightweight properties, are used in automotive and aerospace sectors for parts that benefit from weight reduction without compromising strength. Titanium alloys, especially Ti-6Al-4V, are known for their high strength-to-weight ratio, making them indispensable in aerospace and biomedical implants [12]. Next chapter will focus on Ti-6Al-4V alloy as the tested material in this thesis.

1.2 Additively manufactured Ti-6Al-4V

Titanium alloys offer several benefits that make them attractive for L-PBF applications. Ti-6Al-4V alloy consists of titanium combined with 6 percent of aluminum and 4 percent vanadium, and small amounts of iron and other elements.It is also known as Grade 5 titanium and is the most widely used titanium alloy due to its high strength, light weight, outstanding corrosion resistance, and its ability to withstand high temperatures. These characteristics makes it suitable material for aerospace applications [13]. Beside, the microstructure of Ti-6Al-4V can be manipulated through heat treatment in a way that allows the material to achieve a range of mechanical properties tailored to specific applications. The advent of AM technologies like L-PBF and DMLS, has unlocked new possibilities for fabricated aerospace components that have complex geometries. This layer-by-layer building method allows for the optimization of internal structures of these components [14].

1.3 AM Ti-6Al-4V in Aerospace

Recently the aerospace sector has embraced AM for its capacity to manufacture complex geometrical components which are often challenging or hard to produce through traditional manufacturing methods. A statistical report on Additive Manufacturing research website shows that the aerospace industry accounts for approximately 18.2 percentage of the AM market revenue, which reflect its pivotal role in pioneering applications of this technology.AM capabilities are critical for producing intricate parts such as lightweight structures and engine components which contribute significantly to the efficiency and performance of aerospace vehicles. As the aerospace components are typically made from costly raw material, the recycling process for the scraps produced from these raw material is expensive and requires considerable effort. Traditional machining processes may result in a scrap ratio of 80-90 percent of the original billet, while the AM process can reduce this scrap ratio to about 10 percent [15]. Besides, the AM process allows for the creation of free-form designs that are useful in producing tooling fixtures. In conventional manufacturing, only straight-lined cooling channels are possible, which complicates the optimization of fluid flow in aerospace components [16]. In contrast, AM can create cooling channels with complex geometries that follow the curvature of the part, offering significant advantages for engine components that operate at high temperatures [17]. Another advantage of AM process is its capability to produce multiple aerospace components as one single component. This will lead to a product enhancement which is attained by decreasing the assembly effort and time and make the uncertainties more modifiable and manageable. As an example to this advantage, General Electricity (GE) reduced the number of parts in their fuel nozzle from 20 different parts to one part weighing 25 percent less by using the AM process [18]. When it comes to the economic attributes of additive manufacturing, they are particularly well-suited to aerospace applications, unlike for industries focused on mass production, which simplifies the creation of customized products. Typically, the fly-to-buy ratio the amount of raw material used compared to the final weight of aerospace components ranges from 20:1 to 40:1 [19]. This high ratio indicates a considerable amount of raw material waste, which significantly impacts production costs. By implementing AM techniques, this ratio can be drastically reduced, approaching the optimal 1:1 [20]. For instance, GE Aviation has leveraged AM to produce turbine blades that are not only lighter but also feature advanced internal cooling mechanisms to enhance performance. Similarly, Boeing and Airbus have employed AM to create highly efficient and precisely designed fuel injectors and other critical engine components. A reduction of 50 and 67 percent of the total and production time respectively was claimed by Boeing, this reduction of the part count and installation times lead to reduced inventory pressures and operational costs. As a result, the logistics costs will be lower and there will be more options regarding the selection of suppliers [18].

1.3.1 Challenges

Despite the numerous advantages of additive manufactured Ti-6Al-4V and being a revolutionary technology with the potential to improve a wide range of industries, there are some challenges that need to be addressed for successful and consistent

production of high-quality parts that can be used in weight-critical application like aerospace. This section addresses the key challenges that are associated with AM of Ti-6Al-4V.
Manufacturing of Ti-6Al-4V can be done either with traditional methods that include forging, casting, and machining, which involve shaping the alloy from bulk material through various processes or using additive methods. When compared to traditionally manufactured Ti-6Al-4V, AM Ti-6Al-4V might have lower strength, stiffness, and toughness levels [21]. One deficiency that arises during the AM process from the incomplete melting of the powder particles is porosity. Porosity acts as a stress concentration that reduces mechanical strength and fatigue life of the manufactured part. Another issue results during the AM process is the residual stress which results from the rapid heating and cooling cycles during printing. Having unmanaged residual stress can lead to warping, distortion, and even cracks that affect the fatigue life of the alloy. AM is mainly distinguished by the layer-by-layer nature of the manufacturing. However, this process results in a rougher surface finish compared to traditionally manufactured parts. As a result, some applications require post-processing to improve the surface quality of the AM parts. Yet, the concern about surface roughness of AM parts and how it affects the fatigue strength still arises and will be examined in the following chapters. Having parts that have complex geometries is also a challenge. These parts often require specialized support structures in order to prevent overhanging parts from collapsing during printing. Designing these structures is crucial as it is important to minimize material waste and post-processing time associated with support removal. The concerns are not only about the printing process, there are also some challenges related to Ti-6Al-4V material like the reaction of Ti-6Al-4V with atmospheric gases like oxygen and nitrogen at high temperatures during AM process which leads to the formation of oxides and nitrites within the part [22]. As a result, this affects the mechanical properties of the part negatively. The printing parameters need to be controlled and optimized so that ,for example, the rapid solidification during AM does not lead to a unique microstructure when the printing parameters changes and influence the grain size and phase distribution.

1.4 Research objectives and research questions

The thesis addresses the following research questions:-

1- How can the surface roughness of AM parts be effectively characterized to accurately assess its impact on fatigue life? The thesis investigates methods for effectively characterizing the surface roughness of AM Ti-6Al-4V parts to accurately assess its impact on the fatigue life. In this thesis, the correlation between quantitative surface metrics and fatigue performance will be investigated to identify which surface characteristics are most critical in predicting fatigue failure.

2- What is the influence of the combined factors of surface roughness and geometrical stress concentrations on the fatigue behavior of components? Another aspect that is examined in this thesis is how surface roughness interacts with geometrical stress concentrations to affect the fatigue behavior of components.

3- Does the fatigue behavior treated by hirtisation show consistency

under both constant and variable amplitude loading? If variations exist, what factors contribute to the observed differences? Part of thesis examins the fatigue behavior of specimens treated with hirtisation, comparing their performance under constant and variable amplitude loading. The aim is to determine the fatigue behaviour across different loading regimes and identify the contributing factors to any observed variations in fatigue life.

-What are the characteristics of the fatigue initiation point(s) in AM material, can they be quantified and how do they relate to the overall surface roughness? The thesis focuses on identifying and quantifying the characteristics of fatigue initiation points within the AM material. It investigates how these initiation sites correlate with overall surface roughness and seeks to understand the mechanics behind fatigue crack initiation in relation to the surface condition.

-Can the size (and shape) of the irregularities at initiation points be related to the fatigue life? Further, the study probes whether the size and shape of irregularities at the initiation points can be directly related to the fatigue life of AM parts. This includes a detailed analysis of defect morphology and its role in the initiation and propagation of fatigue cracks.

-What are the characteristics of fatigue crack growth?

The thesis addresses the progression of fatigue cracks, examining whether cracks initiate from the first cycle or after a latency period, the nature of crack propagation (whether multiple small cracks link up or a single lead crack dominates), and how these dynamics vary with different types of loads (tensile or combined tensile/torsion) and load ratios.

2 Literature review

This literature review explores the latest works done to study the relation between surface roughness and fatigue performance. This thesis was inspired by the PhD study [23] that was done by the supervisor of the thesis; Magnus Kahlin. It investigates the fatigue behavior of Ti6Al4V produced using L-PBF and E-PBF with focuses on the effects of geometry, surface roughness, loading conditions, and post-processing techniques on the fatigue life. The study shows that the rough surfaces are the most significant factor reducing fatigue life in AM parts and post-processing methods to refine these surfaces such as shot peening can significantly improve this fatigue strength when it achieves levels comparable to conventionally manufactured Ti6Al4V. Another finding from this study is that L-PBF processed parts with appropriate post-processing can achieve fatigue strengths like conventionally manufactured material. While E-PBF processed parts generally show rougher surfaces and require more extensive post-processing to reach comparable fatigue strengths. Another paper that focuses on the combined effects of rough AB surfaces and geometrical notches on fatigue life [24]. The examination on treating the surface roughness with Hot Isostatic Pressing (HIP) treatment shows that it does not significantly improve the fatigue life for specimens with rough AB surfaces. As well, machining and polishing improve fatigue strength significantly compared to the AB surfaces. It also studied the crack initiation points for the AB surfaces which tend to have multiple crack initiation sites. For machined specimens, cracks initiate both at the surface and internally. One of the findings of this study is that the specimens with notches (Kt= 2.5) show crack initiation primarily at the root of the notch. Part of the previous study was done to evaluates the fatigue behavior under variable amplitude loading and uses the Short-FALSTAFF load sequence to simulate aerospace conditions. It confirmed that conventional cumulative damage approaches (Palmgren-Miner rule) could reliably predict fatigue life for AM materials subjected to tensile-dominated variable amplitude loading sequences like Short-FALSTAFF. The cumulative damage approach predicted fatigue life within a reasonable range, with experimental results generally showing longer fatigue lives than predicted. Another interesting finding is that the notched specimens with Kt= 2.5 had more crack initiation sites compared to un-notched specimens with Kt= 1. The study also demonstrated the feasibility of using constant amplitude fatigue data to predict variable amplitude fatigue life for AM Ti6Al4V. Another study that investigates the fatigue crack growth (FCG) behavior of additive manufactured Ti6Al4V produced by L-PBF [25]. It focuses on comparing the FCG rates of through-thickness cracks in conventional compact tension (CT) specimens with part-through cracks in keyhole specimens. This comparison aims to determine if FCG rates for CT specimens can be applied to damage tolerance analysis for AM parts in aerospace applications. One of the key findings of the study is that the internal defects such as gas pores and lack of fusions were rare, means the dominant factor that impact the fatigue life is the surface roughness. Besides, residual stresses have a major effect on FCG behavior, but heat treatment (at 850°C for 4 hours) minimizes the anisotropic FCG rates.

3 Theory

3.1 Surface roughness

When it comes to 3D printing and any other manufacturing process, there is a distinction between the nominal surface of the part; that is, the intended surface that is dimensioned on a drawing, and the real surface, which is the actual boundary of an object that deviates from the nominal one as a result of the process of creation. This deviation, depends on the properties, composition and structure of the material as well as the manufacturing method. In the case of L-PBF 3D printing, this deviation can be substantial and the roughness of the part can affect the structural properties of the component.

3.1.1 Surface imperfections

Surface roughness is the measure of the total spaced irregularities present on the surface of the part, typically, these are represented in Figure 3 and collected as [26]:

- **Form error**: results in long wavelength deviations from the nominal surface, coming from large scale problems in the manufacturing process like in the machine, guides, alignment.
- **Roughness:** results from the shortest wavelength irregularities of the surface. This is due to a particular production process like layer height in L-PBF 3D printing.
- **Waviness:** includes the longer wavelength deviations from the nominal surface; and although it is in between roughness and form error, it is hard to differentiate from the later one.
- **Lay:** refers to the predominant direction of the surface texture, and it is commonly determined by the production method. While some methods like turning or milling produce surfaces with lay, other methods like sand casting, peening or L-PBF typically have no lay.
- **Surface texture:** results from a short wavelength deviations from the nominal surface. This includes the roughness, the waviness and lay.
- **Flaws:** can be unwanted problems within a surface but usually characterised as individual features.

3.1.2 Parameters

The specification of parameters for surface roughness measurements was collected on ISO 4287-1997 [27] with an updated version on 2021. On this document, parameters were described to avoid being open to different interpretations from users and software developers.

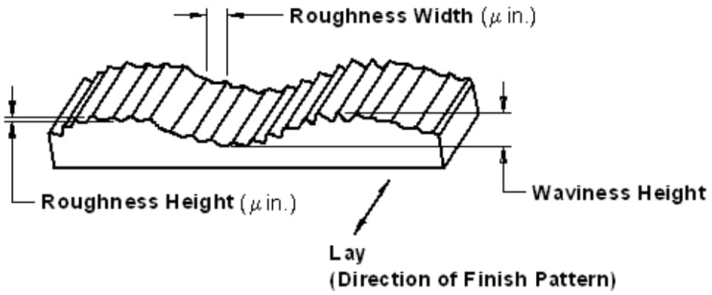

Figure 3: Exaggerated surface imperfections.[26]

Some of the common parameters used in the industry are shown in Table 1, however, from the SEM microscope, only R_a, R_q, R_z, R_p, R_v, R_{sk}, R_{ku}, R_{mr}, R_{dc} and R_c were obtained.

Parameter	**Definition**
Ra	Average Roughness
Rq	Root Mean Square Roughness
Rt	Total Height of the Roughness Profile
Rz	Average Maximum Height of the Profile
Rp	Maximum Peak Height
Rv	Maximum Valley Depth
Rsk	Skewness of the Roughness Profile
Rku	Kurtosis of the Roughness Profile
Rsm	Mean Width of the Profile Elements
Rpc	Profile Peak Count
Rmr(c)	Material Ratio Curve
Rmax	Maximum Roughness Depth
R3z	Average Roughness Depth of Three Segments
Rc	Mean Height of Roughness Component Profile
RzJIS	Ten-point Average Roughness
$R\Delta q$	Root Mean Square Slope of the Roughness Profile
AR	Autocorrelation Length
Rx	Maximum Roughness Depth
Wa	Arithmetical Mean Deviation of the Assessed Profile
Wt	Total Height of the Waviness Profile
Wq	Root Mean Square Waviness
Wsk	Skewness of the Waviness Profile
Wku	Kurtosis of the Waviness Profile

Table 1: Surface Roughness Parameters and Definitions

To be able to assess the impact of surface roughness on fatigue behavior, surface roughness parameters needed to be chosen carefully from Table 1 based on an analysis of their correlation with fatigue life and various aspects of surface texture. A key surface roughness parameter to study is the average value of the roughness. Thus, R_a would be the suitable parameter as it gives the the average vertical devi-

ation of the peaks and valleys from the mean line. However, it may not adequately describe the effects of extreme peaks or valleys and also not fully accurate as some valley values might cancel some peak values. R_q is similar to R_a but gives more weight to higher peaks and deeper valleys as it is the root mean square of the profile heights, which means it can be more sensitive to surface irregularities than R_a. Another important parameter that gives information about the effects of extreme values that are critical to the performance of the material is R_z which represents the average distance between the highest peak and the lowest valley in several sampling lengths. Also, it is important to analyse the depth of the deepest valley R_v as well as analysing the height of the highest peak R_p. However, R_v is more critical to study as after analysing the surface fracture points, it was noticed that almost all of the intuition points happen at the valleys which makes sense as it acts as stress concentrators or as an existing crack in the material [28].

3.1.3 Hirtisation surface treatment

As the additive manufactured specimens that are printed using L-PBF often have rougher as-built surface, postprocessing treatment should be employed to enhance the quality of these surfaces. Many techniques can be used to improve the surface roughness like electrolytic polishing, sandblasting, and tumble finishing [29]. In this thesis, some of the tested specimens will be examined in their as-built condition. Nevertheless, some specimens will be post processed using hirtisation which is a post-processing technique which enhances the surface quality of specimens with high-performance materials. The process of hirtisation is done with many steps that involves a combination of chemical and electro-chemical treatments which leads to smooth and refine the surface of metal parts. This process achieves the removal of the unwanted material and smooth the surface without compromising the component's dimensional integrity. The steps of hirtisation start by a chemical treatment of the specimen though putting it in a specially formulated chemical solution which is designed to dissolve high points on the surface and partially melt particles. Then the second step is the electrochemical process which further smooths the surface by selectively dissolving the high points of the surface roughness when it is put in electrolyte solution. The last step is that the part undergoes a hydrodynamic process that involves fluid flow to ensure uniform treatment and the removal of dissolved materials [30]. Compared to other methods like sandblasting or traditional chemical polishing, hirtisation offers a more uniform and thorough surface finish [31].

3.2 Key printing parameters

In additive manufacturing, printing parameters like laser power, scanning speed, layer thickness, and hatch spacing significantly influence the printing process's outcome. Therefore it is important to define and optimise the important parameters as they will have an effect in the microstructure, mechanical properties, and surface quality of the final Ti-6Al-4V parts [32].

Layer thickness

This parameter defines the thickness of each deposited powder layer. Having thinner

layer offers higher resolution and detail, but requires more layers to build the part, increasing printing time. On the other hand, a thicker layer allows for faster printing but can negatively impact surface finish and mechanical properties.

Laser power
Laser beam power dictates the amount of energy delivered to the powder bed. Having higher power leads to deeper melt pools and increased melting efficiency. However, excessive power can lead to defects like porosity or thermal deformation and can also result in residual stress and warping. The optimal power setting depends on the specific AM process and equipment used to achieve the desired material characteristics and part quality.

Powder size
The powder size parameter refers to the diameter of the powder particles used in the printing process. This parameter significantly influences the powder's flowability, packing density, energy absorption from the laser or electron beam, and ultimately the surface finish and mechanical properties of the final part.

Hatch distance
This distance refers to the distance between adjacent laser scan lines or electron beam paths within a single layer. This distance is important to be known as having a narrower hatch spacing ensures better layer-to-layer bonding but reduces printing speed. Unlikely, wider spacing increases printing speed but can lead to porosity and weak inter-layer bonding.

3.3 Fatigue

Fatigue is a common source of failure in materials that occurs over a long period of time when exposed to cyclic loading. This kind of failure, occurs with loads below the ultimate strength of the material as cracks start to form and slowly grow over the section of the component. In aviation, the predominant kinds of fatigue are Low-Cycle Fatigue (LCF), High-Cycle Fatigue (HCF) and Thermo-Mechanical Fatigue (TMF).
In this thesis work however, only HCF will be investigated, with number of cycles to failure ranging from 10^4 to 10^6.

3.3.1 Crack growth

Fatigue is usually defined as the deterioration of a component caused by the crack initiation and growth. There are three stages of the process commonly characterized as:

- **Crack initiation:** One crack becomes dominant and other micro-cracks start to interact after an initiation process as suggested by [33]. It is not detectable with the naked eye and it is a stage characterized by the tangent stresses. Micro-cracks form at the surface due to the formation of extrusions and intrusions in the slip bands and these (Figure 4) start to grow.

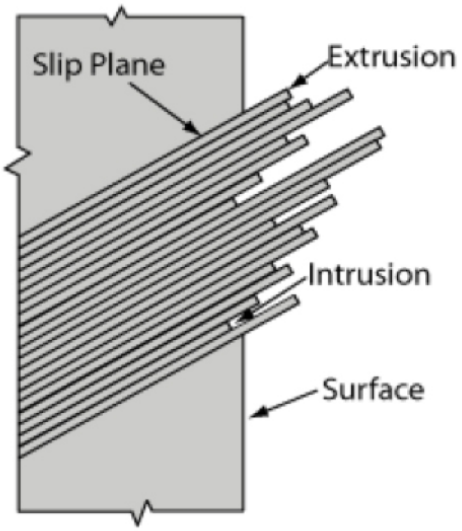

Figure 4: Slip bands.

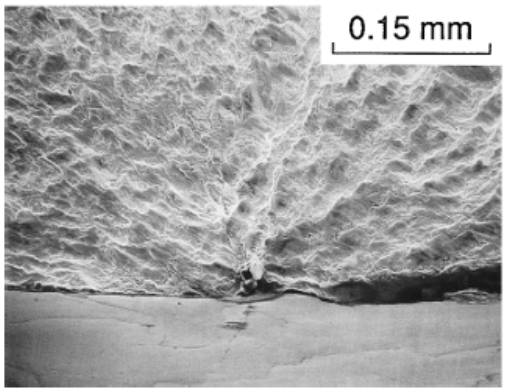

Figure 5: Inclusion in material with river marks.

- **Crack propagation:** In this stage, the crack start to grow due to the local stresses characterized by tangent stresses and normal to the principal stress direction. In this stage the crack can start to be seen by the naked eye. The surface left on the specimen will be smooth and shiny without any clear plastic deformation evidence although benchmarks could appear if exposed to a change in amplitude.

- **Final fracture:** It is the stage where a quick propagation occurs as the crack driving force exceed the fracture toughness of the material. It is also dominated by the tangent stress and will make thus, the border between the smooth fatigue fracture surface and the plastic deformation from the final fracture.

3.3.2 Fatigue loading

Cyclic loading can come from many types of load, nevertheless, all fluctuating loads have to be considered. In the industry, load can come from applied loads, dead weights, wind load, fluid pressure, temperature variations and multiple others. The resulting stresses on the component will eventually lead to fatigue failure given the proper conditions.
Generally, cyclic loading is generally divided in two categories; constant amplitude (CA) as seen in Figure 6 and variable amplitude (VA) as seen in Figure 7. The latter, will be analyzed in subsubsection 3.3.5, but it implies that the cyclic load varies in magnitude over the time the test is performed. Constant amplitude however, implies that the specimens are exposed to a sinusoidal stress variation. It can have a positive or negative average, but it has a constant amplitude over such average. Depending on the average and maximum and minimums of the stress applied, it will have a specific stress ratio.

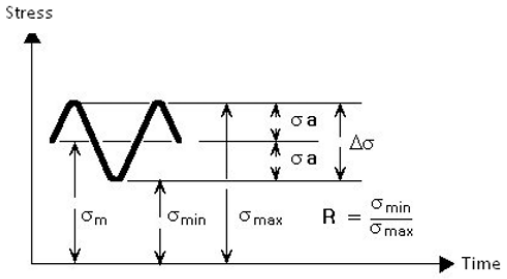

Figure 6: Constant amplitude stress variation.

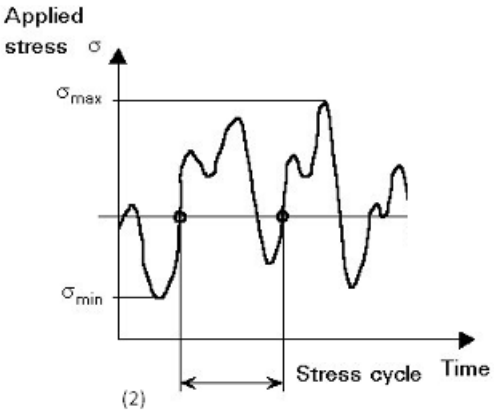

Figure 7: Variable amplitude stress variation.

Commonly, CA fatigue stress cycles are characterized by the following quantities:

- Stress ratio (R), is the ratio between the minimum and maximum stress as:

$$R = \frac{\sigma_{min}}{\sigma_{max}}$$

- Stress range ($\Delta\sigma$), is the difference between the maximum and minimum stress:

$$\Delta\sigma = \sigma_{max} - \sigma_{min}$$

- Stress amplitude (σ_a), is defined as half of the stress range:

$$\sigma_a = \frac{\Delta\sigma}{2}$$

- Mean stress (σ_m), defined as the average between the maximum and minimum stress:

$$\sigma_m = \frac{\sigma_{max} + \sigma_{min}}{2}$$

Fatigue life of metallic materials depends strongly on the applied stress range. Moreover, for a constant stress range, the fatigue life is decreased by increasing the stress ratio (R). While fatigue can be of different types like bending, shear, fretting or normal; in this thesis, only normal stresses will be applied.

3.3.3 Wöhler (S-N) curves

SN-curves, were introduced by German scientist August Wöhler in 1842; were fatigue test are plotted with the magnitude of alternating stress against the logarithm of number of cycles to failure [34].
A considerable number of tests needs to be performed to produce one curve. Some materials, like steel for instance, have a distinct endurance limit, below which, no fatigue failure takes place.

3.3.4 Stress concentrations

Stress concentrations will appear when the shape of a component becomes irregular, this can be due to the geometry of the component including area changes, corners, holes or due to cracks, notches or defects both on the surface or in the specimen. These spots where stress concentration is the highest, will most likely result in the initiation of cracks due to fatigue loading if not designed properly.

The stress concentration factor (K_t) is defined as the maximum stress (σ_{max}) at the stress concentration point, to a nominal stress (σ_{nom}):

$$K_t = \frac{\sigma_{max}}{\sigma_{nom}} \tag{1}$$

In this study, both specimens with and without notch are tested, and the respective stress concentration factors are presented in subsubsection 4.2.1

Stress concentration factors can be obtained from handbooks like Peterson's diagrams [35] or computed using, for example FEA. However, this is out of the scope of this work so the stress concentration factors used are only the ones given by Saab in subsubsection 4.2.1.

3.3.5 Aircraft spectrum for fatigue loading

The variable amplitude test were performed using variable amplitude loading with a modified fighter aircraft wing bending spectrum Short-FALSTAFF (Short Fighter Aircraft Loading STAndard For Fatigue), which reduced the fatigue test times from the original FALSTAFF proposed by NLR-Netherlands, LBF-Germany, IABG-Germany and F&W-Switzerland [36].

The reduced time comes from a reduction of around 50% of the number of cycles, but nevertheless, the accumulative damage performed by the modified version comes near the one from the original FALSTAFF load sequence. The modified version was developed by CEAT in Toulouse [37].

The load sequence of the Short-FALSTAFF spectrum and the distribution of peaks and troughs are represented in Figure 8 by [24], were the maximum tensile peak (100) correspond to the maximum net section peak stress used for variable amplitude tests, which in the case of this thesis, are either 670 or 910 MPa.

The sequence runs then repeatedly during a fatigue test until the specimen fails. One sequence consists of 18,012 turning points, which corresponds to 200 simulated flights. So, having the elapsed time of the test until the specimen fails, one can calculate the total number of flights with:

$$N^{\circ}{}_{flights} = \frac{T_{elapsed} \cdot 10}{18012} \cdot 200 \tag{2}$$

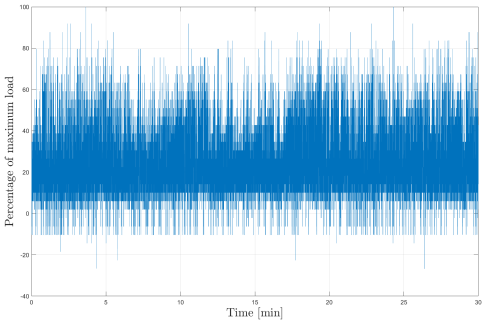

One sequence of the Short-FALSTAFF load spectrum.

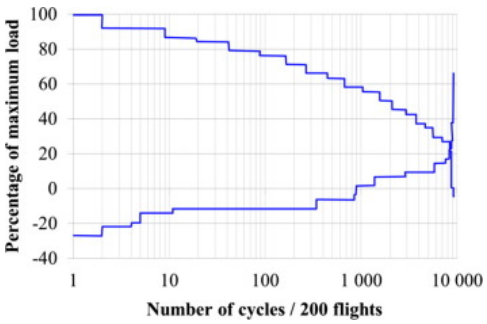

Distribution of peaks and troughs for one Short-FALSTAFF load sequence.

Figure 8: Short-FALSTAFF spectrum characterized.

3.3.6 Rainflow counting

The rainflow counting (RFC) method is a technique used to calculate cycles from a sequence of reversal points. RFC produces a list of full cycles with their corresponding stress ranges and number of occurrences. As specified in ASTM E1049-85 guide for cycles counting, the idea is to count a range as a cycle if it can be paired with a subsequent loading in the opposite direction. This results in a simple algorithm described as follows, where n is the current range and $n-1$ is the preceding range and the procedure can be seen in Figure 9:

- 1. Read next peak or valley. If out of data, go to Step 5.
- 2. If there are less than three points, go to Step 1. Form ranges$n$ and $n-1$ using the three most recent points (i.e., peak and valley) that have not been discarded.
- 3. Compare the absolute magnitude of range n to that of range $n-1$:
  - If $|n| < |n-1|$ go to Step 1.
  - If $|n| \geq |n-1|$ go to Step 4.
- 4. Count range $n-1$ as one cycle and discard the points that define it.
- 5. If any cycles remain, start at the end of the sequence and count backwards. If a single peak remains, count it as one cycle.

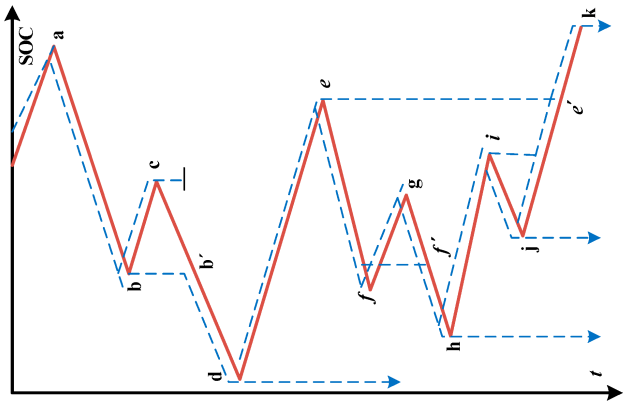

Figure 9: Rainflow counting cycles methodology

When it comes to the spectrum in subsubsection 3.3.5, for the Short-FALSTAFF a total of 18,012 turning points were identified, and after running the rainflow counting algorithm, a total of 9,005.5 cycles were identified, where the half cycles comes as not another reversal could be identified to complete the cycle. From those cycles, there are 170 unique cycles with different mean and alternating stresses. The histogram for the spectrum is represented in Figure 10, were the cumulative density of cycles is plotted against the stress range $(2 \cdot \sigma_a)$.

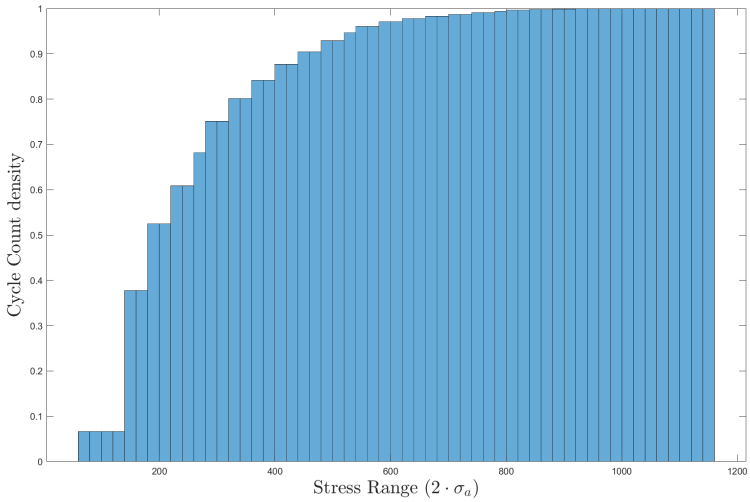

Figure 10: Histogram for Short-FALSTAFF spectrum.

3.3.7 Haigh diagram

The Haigh diagram, is a convenient plot for the engineer as S-N or Wöhler curves only apply for fatigue tests with a specific stress ratio. However, components are usually dynamically loaded, so to properly assess the fatigue life of a component, many more Wöhler curves would be needed. That is why special diagrams like the Haigh diagram are used to illustrate the influence of the mean stress. In it, the alternating stress is plotted against the mean stress of the cycle

For the whole spectrum, a Haigh diagram can be plotted as seen in Figure 11, were each specific cycle has been plotted with the specific mean and alternating

stress. Each cycle, has a different color indicating the amount of times that it is repeated along the Short-FALSTAFF spectrum. In the figure, one can also distinguish 4 different stress ratio curves, this will be useful in the following section where a fatigue life prediction has been made for the variable amplitude specimens using constant amplitude data. One could also plot the Goodman line indicating the endurance limit for the different sections of the diagram, going from the endurance limit in the vertical axis ($R = -1$) to the ultimate tensile strength in the horizontal axis, which would represent a static test. However, due to the amount of specimens available in this project, such endurance limit and ultimate tensile strength were not possible to be determined; nevertheless, reference values were obtained from [23] and thus, such Goodman line is plotted in green in Figure 11.

The theory from the Goodman line is that any cycle that lies below the curve, will make the specimen survive for the given alternating and mean stress. If however, lies above it, the specimen will eventually fail for the given conditions.

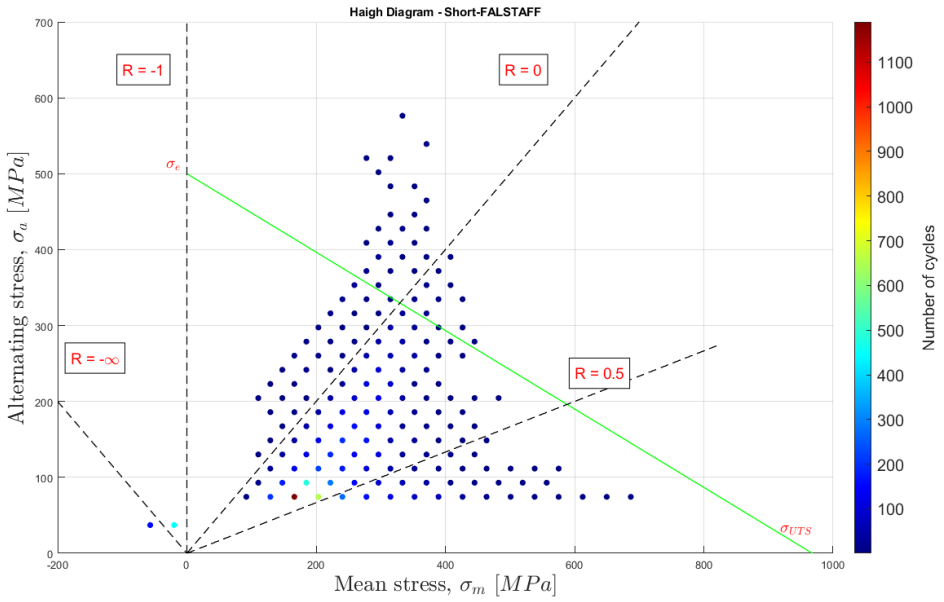

Figure 11: Haigh Diagram for Ti-6Al-4V with Short-FALSTAFF cycles with 910 MPa **maximum stress.**

Most of the cycles lay below the Goodman curve, and thus, will not make the specimen fail. However, as the spectrum from subsubsection 3.3.5 has multiple cycles above the curve, it will fail eventually. Note also that there are two compressive cycles, which would "close" the crack providing even further life to the specimens. Even if a cycles lays below the Goodman line, it can still produce damage to the specimen, however, if for that stress level the cycles to failure are higher than $> 10^6$ cycles, it is usually acknowledged as if that stress level has no influence.

3.3.8 Cumulative damage approach

A basic problem in fatigue research is the prediction of fatigue life of specimens or components when a variable amplitude spectrum is applied. Usually, fatigue tests are preformed with constant amplitude, resulting in the number of cycles-to-failure or (N_f) for a given stress amplitude. The problem for this variable spectrum resides in determining the number of cycles under this loading program. [38]

The cumulative damage approach theory is deterministic, thus it ignores the considerable scatter of the fatigue test data; therefore, all results from constant amplitude are curve fitted. A basic concept in the approach is the damage function which determines in some sense, the "damage" produced to the specimen or component when a specific cycles is applied n times with a stress amplitude σ_a. It is often written as $F(\frac{n}{N})$ where N is the cycles to failure for constant amplitude at σ_a loading.

One of the most well-known damage functions was postulated by Palmgren and Miner, where failure would occur when the function equals to one. Resulting thus, for a VA spectrum as:

$$\sum_i \frac{n_i}{N_i} = 1 \tag{3}$$

where n_i is the number of cycles at loading σ_i and N_i the cycles to failure at constant amplitude σ_i. According to this rule, the individual damages are additive and independent of sequence; however, this simplistic approach does not comply always with reality, and there are other methods like Miner's coefficient that could better predict failure. However, due to the resources for this project, the simplistic approach will be used as a reference of what could be done if more data was available[38] .

With this approach, one could then calculate the number of times the spectrum can be applied to the specimens as:

$$\frac{1}{\sum_i \frac{n_i}{N_i}} = 1 \tag{4}$$

As mentioned in subsubsection 3.3.5, 910 and 670 MPa maximum loads were applied in the spectrum. This results in the highest load being of such stress but the rest of the specific cycles being adjusted accordingly.

Multiplying finally the number of cycles by 200 as seen in subsubsection 3.3.5, the predicted number of flights for the maximum stress applied would be determined.

3.4 Material

Ti-6Al-4V is the most widely used titanium alloy produced corresponding to over 50% of the annual production [23]; being the aerospace and medical industry the two major consumers.

The AM Ti-6Al-4V has the same chemical composition as the one produced by conventional methods like casting, bar or forging. In Table 2, the maximum and minimum percentage of each element is shown.

	Al	V	Fe	O	C	N	H	Y	Other	Ti
Min, [%]	5.5	3.5	-	-	-	-	-	-	-	Remainder
Max, [%]	6.75	4.5	0.3	0.2	0.08	0.05	0.015	0.005	0.4	

Table 2: Chemical composition according to ASTM F2924-14, for Ti-6Al-4V manufactured by powder bed fusion. [23]

3.4.1 Microstructure

AM PBF production methods involve layer deposition by a consequent melting of the particles; which involves both heating and rapid cooling of the material. This in turn, limits the growth of the grains as they do not have enough time to grow due to the quick cooling rates of around 10^4 K/s [23].
For each layer, the laser melts both the new deposited layer as well as several layers below depending on the layer size; giving in turn, a continuous microstructure across the layers and promoting columnar grain structure growth along the vertical building direction [23].

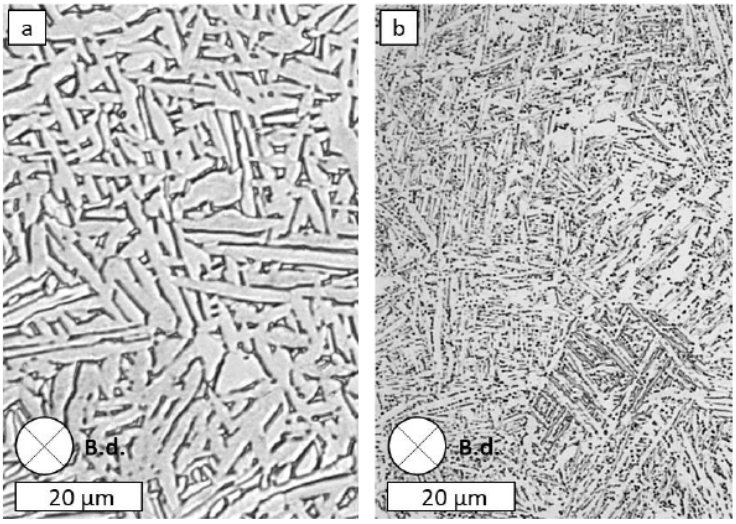

Figure 12: Typical microstructure of Ti-6Al-4V manufactured by E-PBF (HIPed) a) and L-PBF (stress relieved) b) [23].

In the case of L-PBF produced Ti-6Al-4V, as seen in Figure 12 (b), due to the previously mentioned cooling rates, a finer microstructure is obtained compared to other methods like E-PBF which have a lower cooling rate (Figure 12 (a)). This also contributes to higher residual stresses if no post heat treatment is performed. In the case of the specimens in this thesis, they have been heat treated at $650°C$ for three hours.
Figure 12 shows a columnar grain structure in the vertical build direction with fine and equiaxed grains closer to the surface [23]. Without heat treatment, the microstructure will mainly consist of $\alpha - \alpha'$ (martensite); however, with enough temperature and long heat treatment time, it can become martensitic α', a mixture of $\alpha + \beta$ [23].

4 Method

4.1 Printing parameters

The properties of the finished Ti-6Al-4V specimens are significantly influenced by the selection and optimization of printing parameters. These parameters affect density of the specimens, the mechanical properties, residual stress and most importantly surface roughness. The selection of printing parameters are shown in Table 3:

Parameters \Specimens	**Hirtisation**	**As Built**
Printer	EOS M 290 LS	EOS M 290 LS
Layer thickness $[\mu m]$	30	60 and 30
Powder size $[\mu m]$	50	15 - 53
Laser power $[W]$	n.a.	950
Hatch distance $[mm]$	n.a.	0.12
HIP	650 $°C$ for 3 hours	650 $°C$ for 3 hours

Table 3: The printing parameters of the test specimens

4.2 Testing

For the fatigue tests, a servo hydraulic fatigue test rig with an Instron ± 100 kN load cell and an Instron 8801 control system has been used as seen in Figure 13.

Both constant amplitude and variable amplitude test where performed; on this hydraulic rig. The different load levels are shown in Table 5 and Table 6 for both constant and variable amplitude and different treatments.

For the variable amplitude test, the Short-FALSTAFF spectrum (subsubsection 3.3.5) was imported and only two cases were considered. For the batch $A:3$, an extensometer was used to measure the % of extension of the specimen during the test, the setup of the mentioned system is shown in Figure 14.

Static tensile test for the second print of specimens was also performed in a different Instron hydraulic system. The tensile tests were performed to verify the static properties of the specimen batch or print as it can vary depending on the metal powder used. The test specimens were $A3:1$ type.

An extensometer was used during the first part of the test to measure the strain or relative displacement up to the yield strength at 0.2% offset. The test specimens were loaded with a rate of 0.0045 mm/s according to instructions in test standard ISO 6892-1.

Figure 13: Generic servo hydraulic fatigue test rig 8801 [39].

The extensometer used is manufactured by Instron, with a catalog number of 2620-604 having a range of +12.5 to −2.5 mm. It was then secured with two rubber bands that go around the specimen and clamp tightly to the extensometer. The notch was left in between both clamps and once secured, the safety pin indicating the 0% extension was then removed. However, due to the setup of the rubber bands, the clamps could slide giving non zero values. This however was fixed by shifting the average for the first measurement is shifted to a zero average.

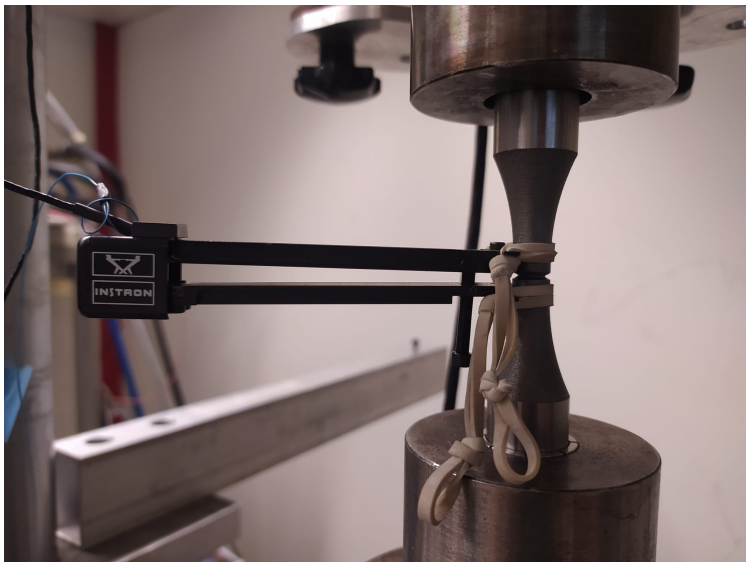

Figure 14: Extensometer setup for a $A:3$ specimen.

4.2.1 Specimens

Several specimen types have been tested, with some outer dimensions, as shown in Figure 15, but with different notch geometries. From having no notch at all, resulting thus, in a K_t of 1 as it is simply a circular section of the specimen, to having different radii like the geometries represented in Figure 15, resulting in values of K_t of 2.2 and 3.

The specimen id, surface conditions, notch conditions, and testing load for each specimen are summarized in Table 4.

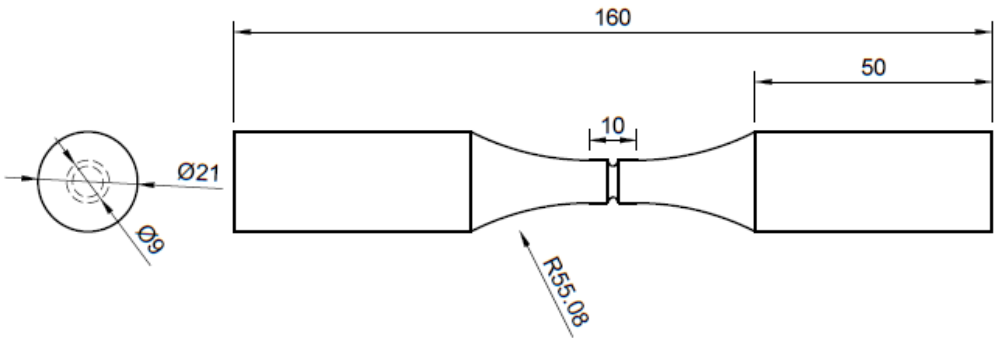

Figure 15: The general geometry of the specimens

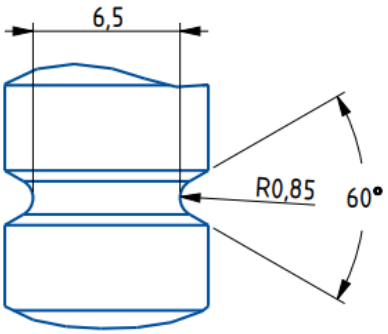

*A*2.2 - **Notch geometry for** $K_t = 2.2$

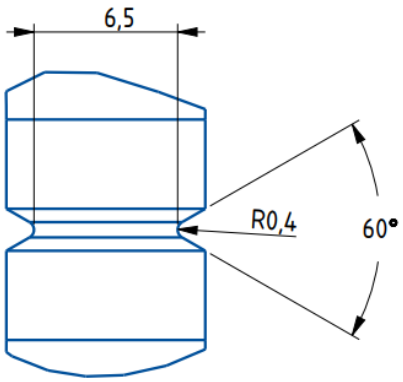

*A*3 - **Notch geometry for** $K_t = 3$

Figure 16: Notch geometries for specimens *A*2.2 **and** *A*3**.**

Specimen id	K_t	**Surface cond.**	**Notch**	**Test**	**Notch R.** $[mm]$
H1, H1.1, H2.1, H6	1	Hirt.	No notch	CA	-
H4, H5, H7, H3	1	Hirt.	No notch	VA	-
A1 x 3	1	AB	No notch	Static	-
A2.2 x 18	2.2	AB	Notched	CA	0.85
A3 x 27	3	AB	Notched	CA	0.65

Table 4: Summary of the test specimens used.

4.2.2 Test conditions

All specimens were tested in load control at ambient lab temperature. Table 5 and Table 6 show the load ratio and applied stresses for hirtisation and as-built specimens, respectively.

Specimen id	**Test**	**Load Ratio**	**Max stress** $[MPa]$
H1.1	CA	0.1	800
H1	CA	0.1	750
H6	CA	0.1	650
H2.1	CA	0.1	500
H4, H3	VA	-	670
H7, H5	VA	-	910

Table 5: Test matrix for hirtisation specimens without notches for CA and VA testing.

Specimen type	**N° spec.**	**Test**	**Load Ratio**
A1	3	Static	-
A2.2	9	CA	-1
A3	9	CA	-1
A3	9	CA	0.1
A3	9	CA	$\sigma_{min} = 200\ MPa$

Table 6: Test matrix for AB specimens.

4.2.3 Test data

The data obtained from the constant amplitude test; is the number of cycles performed until fracture occurs (N_f), as well as the maximum and minimum load applied to the specimen. In the case of the variable amplitude specimens, the elapsed time of the test and the loads were recorded. For the static tensile tests, the stress as well as the strain were recorded and used to determine the elastic modulus, yield strength, ultimate tensile strength and fracture strain.

4.3 Stereo-microscope analysis

Once the fatigue test were performed, an analysis of the fracture surfaces and the defect that caused such initiation was performed in a Leica M205C stereo microscope (Figure 19). The microscope was mounted with a Leica MC170 HD Camera to capture the images with 5 Mpixels providing also with full color images. [40]

The purpose of this analysis was to perform a characterization of the fracture surface. The surface was further analyzed in more detail with the Scanning Electron Microscope with more detail in order to try to determine a relation between the size and shape of defects and the surface roughness measured from the profile.

4.4 Fatigue crack surface characterization

To facilitate an automated analysis of the stereo-microscope images of the crack surfaces, a Matlab Gui App was designed. Figure 17 shows an image in the app.
As shown in Figure 17, the app enables for scaling the image, control of specimen radius and measurement of the fatigue crack size. The crack shape is assume to be elliptic with the in-depth length (a) and a surface length (c), as shown in Figure 18.
One approach to analyze the specimens after they have been tested is with a Stereo-microscope as seen in the previous section, where initiation points notches and rivers are identified.
However, to further characterize such fracture surfaces, a Matlab Gui App was designed to do so in a quickly and a standard way. In the app, the shape and size of the crack can be controlled by sliders at the bottom as shown in Figure 17.

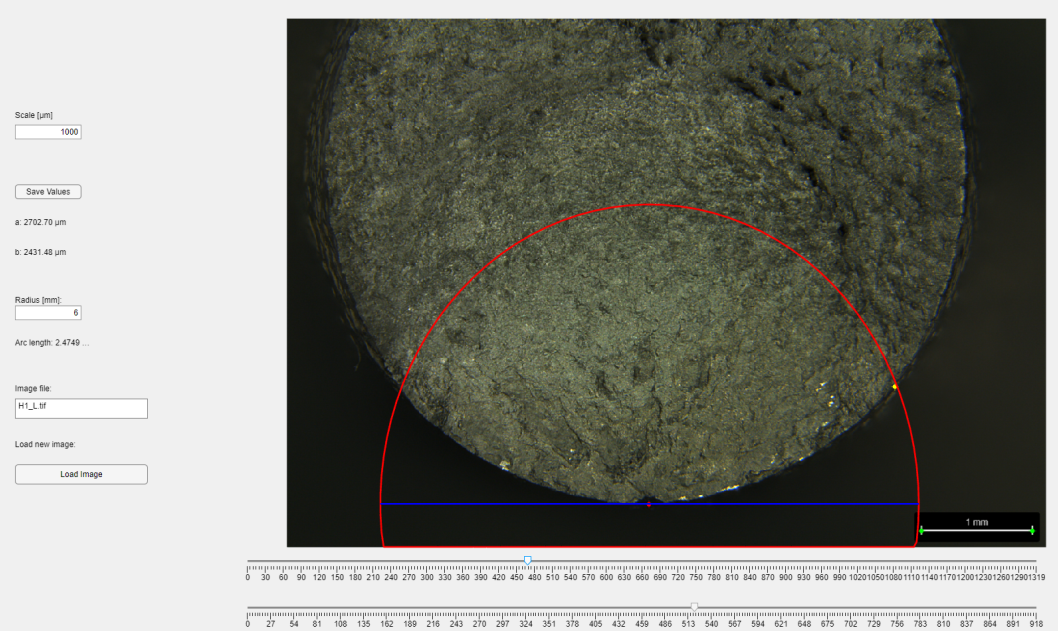

Figure 17: Matlab gui App design to characterize the images.

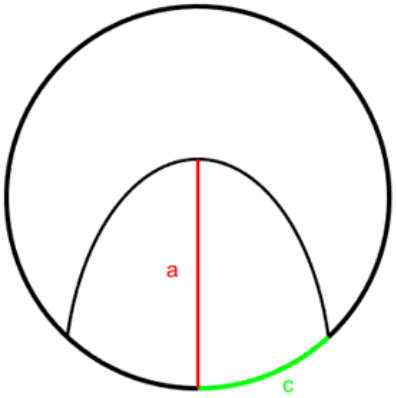

Figure 18: Fatigue crack shape and size.

Characterizing the fatigue fracture surface this way, allows to determine if the crack grows quicker in the depth or spanwise direction. However, this is useful for cracks that initiated in one spot only or with multiple close ones. If however, there are multiple crack initiations along the area of the specimen, then there would be a combination of ellipses and it would be piontless to characterize it this way.

4.5 Surface roughness measurements

The surface roughness parameters of the specimens were measured using a stylus profilometer. The profilometer traces the surface with a thin and sharp tip ("stylus") while recording the "Z" position of it. The tip is usually made of diamond and as it is a finite tip, it will not be able to trace the surface perfectly. This could result

in not capturing really sharp vallies , so it should be taken into account that the measurement is a "filtered" image of the surface [41].

The profilometer used in this thesis is the Mitutoyo SJ-410 can be seen in (Figure 19).

For the specimens without notches, a cut-off length of $\lambda_s = 2.5\ mm$ was selected with 3 sampling intervals. This selection could not be increased as the area starts with the curvature of the gripping part and ends with the notch, and the measurement was intended only in the surface of the specimens. If this range is wanted to be increased, it would be hard not to confuse between the exact points of the curved and flat part in order to apply a profile filter.

The rest of the main parameters were set to $\lambda_C = 8\ \mu m$, with a measuring speed of $M_{speed} = 0.1\ mm/s$ and with a Gauss filter applied for the roughness measurements. These parameter were chosen based on experimental trials and recommendations from experts in the lab.

In the case of the specimens with notches, the cut-off length was set the same with a decrease of the sampling intervals to 2 as only 5 mm were available in this case for the flat part of the surface. However, the notch was measured applying a circular profile filter before the testing in order to capture the roughness, and most likely the defect or deepest valley were crack initiation occured.

Leica M205C Stereo-Microscope. [40]

Mitutoyo SJ-410 profilometer. [42]

Figure 19: Stereo-Microscope and profilometer for analysis.

Surface roughness was measured by a stylus profilometer, however, it was not possible to measure the As-built specimens with the profilometer due to geometry and setup limitations. The AB specimens have bigger gripping area, which prevent the stylus arm from reaching the desired area for measuring. Also, the surface roughness in the notches needed to be measured which was not possible to do with the stylus setup. Thus, another method needed to be used in order to measure the surface roughness on these specimens. The SEM microscope was used to measure the surface roughness for the As-built surfaces and notch. However, to be able to compare the SR results of the hirtisation specimens and the As-built ones, a validation of this method was needed.

4.6 Validation of the surface roughness results

Two different specimens with both cylindrical and square geometries, shown in Figure 20, were measured with both stylus profilometer and SEM.

Figure 20: Cylindrical and flat specimens that were used for SR validation

For both specimens, the measured area where fixed and 10 measurements were performed with the same length (2.5 mm).The average was taken for the 10 measurements and a comparison was done to see the difference between the two methods. As shown in Table 8 and Table 7, the SR parameters for both samples are close when measured using SEM or the Stylus. Nevertheless, the SEM results always show somewhat higher values than the one that is measured by the stylus. Which could be a consequence of the relatively big Stylus needle that can not reach all the deep somewhat valleys which results in not have a very accurate scanning of the stylus. However, the overall conclusion is that SEM can be used to measure SR of the As-built specimens and the results can be comparable with the results of the hirtisation specimens.

Parameter	SEM	Stylus	$\Delta Diff.$ [%]
Ra µm	23.28	21.55	7.43
Rq µm	31.1	26.35	15.27
Rz µm	132.6	128.00	19.80
Rp µm	67.62	61.39	29.94
Rv µm	71.93	66.61	7.40
Rsk	0.4628	-0.05	110.80
Rkµ	2.73	2.61	4.40
Rmr %	0.179	0.14	21.79
Rdc µm	22.14	14.50	78.40
Rc µm	86.98	75.79	21.85

Table 7: SR parameter for the flat sample measured by SEM and the Stylus

Parameter	SEM	Stylus	$\Delta Diff.$ [%]
Ra µm	23.24	22.951	1.24
Rq µm	28.01	28.6846	2.41
Rz µm	130.1	142.9504	9.88
Rp µm	59.3	66.1378	11.53
Rv µm	76.56	76.8126	0.33
Rsk	-0.121	-0.1658	37.02
Rkµ	2.64	2.8006	6.08
Rmr %	0.095	0.076	20.00
Rdc µm	19.56	17.3458	11.32
Rc µm	77.95	86.2744	10.68

Table 8: SR parameter for the cylindrical sample measured by SEM and the Stylus

5 Results

5.1 Surface roughness measurements

It was interesting to know the asymmetry of the surface profile by analysing the R_{sk} or the Skewness parameter. Which is helpful to know as it indicate whether the specimens have more prevalent valleys or peaks. As shown in Figure 22, Figure 21,and Figure 23, all the specimens have positive skew values which indicates that the peaks are dominant over the valleys.

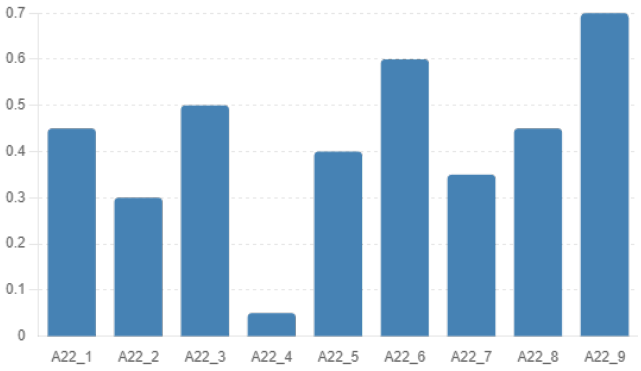

Figure 21: The R_{sk} values for $A2$ specimens

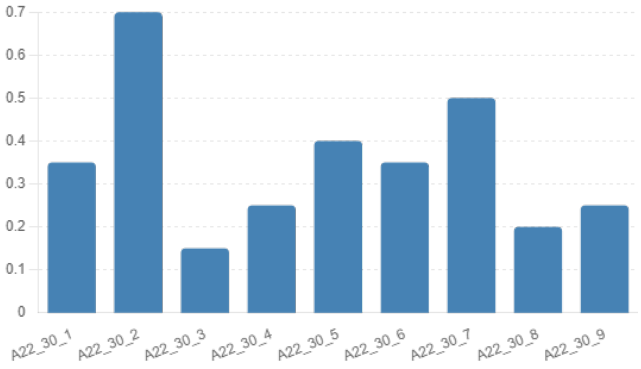

Figure 22: The R_{sk} values for$A2-30$ specimens

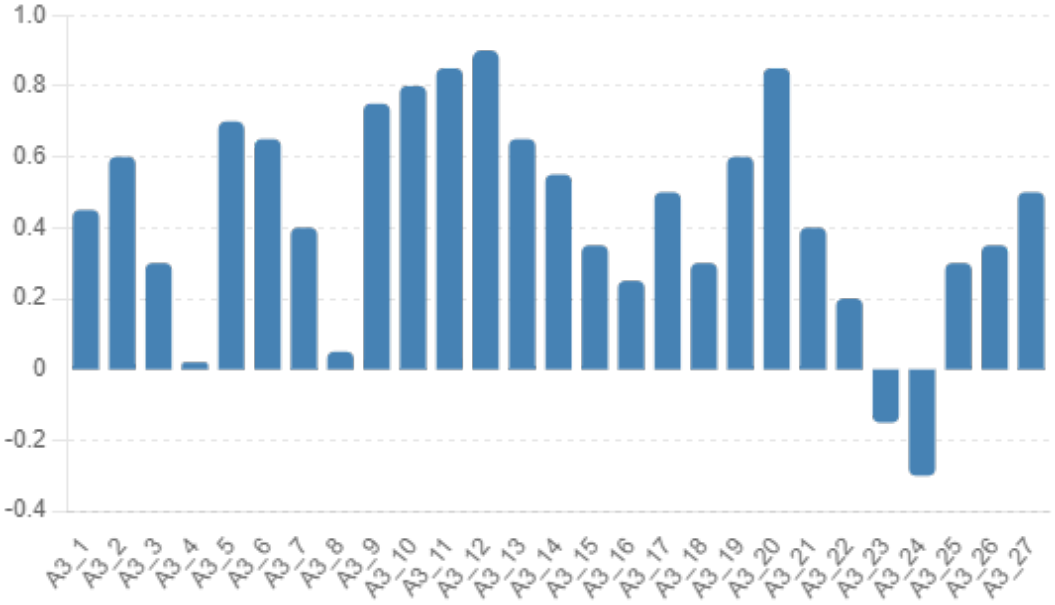

Figure 23: The R_{sk} values for $A3$ specimens

5.2 The impact hirtisation on Surface Roughness and fatigue life

Figure 24 shows the significant difference between the R_v and R_p parameters of the hirtisation treated and AB specimens. In additional to the numbers, the difference can be already noticed on the macro level between Figure 25 (a) and Figure 25 (b).

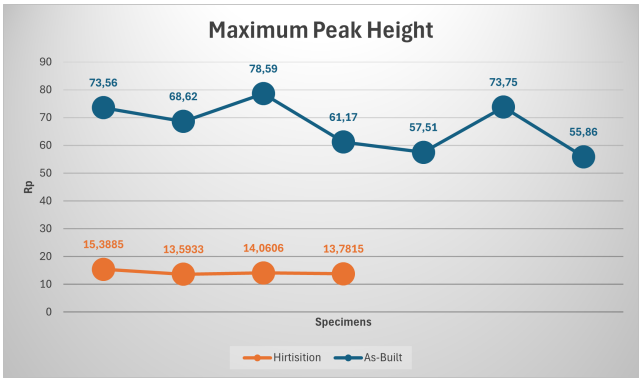

R_p $[\mu m]$

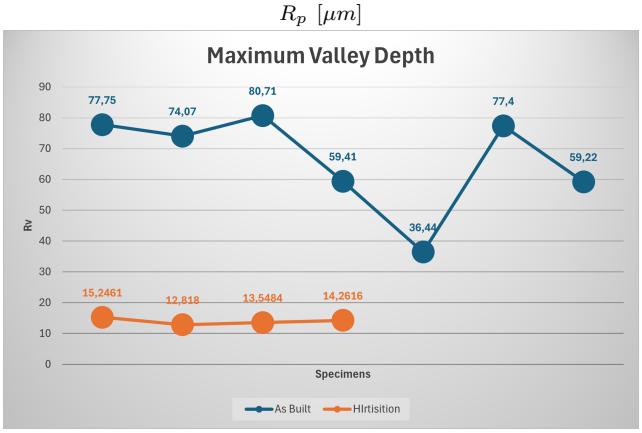

R_v $[\mu m]$

Figure 24: R_v and R_p values of the hirtisated and as-built specimens

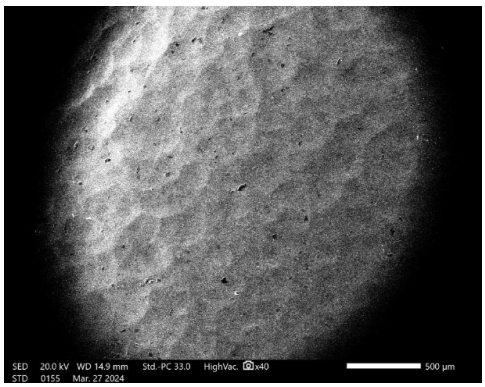

The surface of hirtisation specimens. (a)

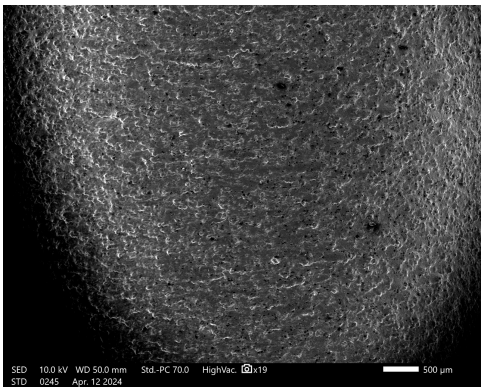

The surface of As-built specimens. (b)

Figure 25: Hirtisated and as-built specimens surface

Figure 26 shows that surface roughness parameters have significant reduction between 75 to 80 percent of their original values before the treatment. In comparison with the following studies, [43], [44] [45], and [46], hirtisation exhibits better impact in improving the surface roughness quality compared to the other post-processing treatment like Chemical Polishing that reduce the roughness by 40-60%, Electrolytic Polishing which reduce the roughness by 60-80%, Sandblasting with a roughness reduction by 30-50% , and finally Tumble Finishing that reduce the roughness by

50-70%.

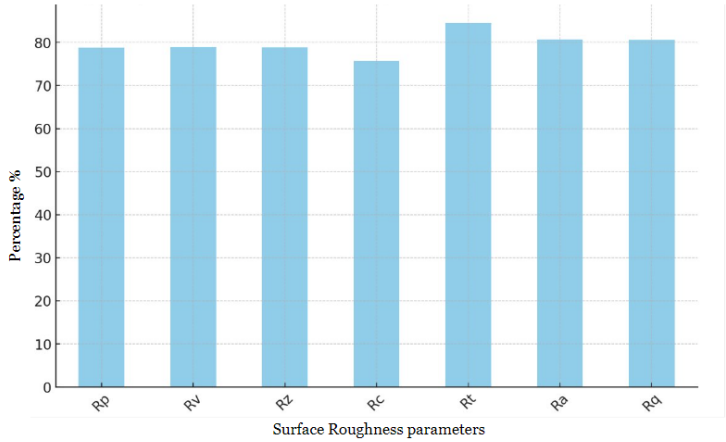

Figure 26: Percentage of reduction in surface roughness parameters between the as-built and the treated with hirtisation

Figure 27 shows the impact of hirtisation on the fatigue life of different specimens. The hirtisation specimens have similar fatigue behavior as the machined specimens which is promising for potential application. Also, AB specimens show a significant decrease in fatigue life compared to machined and hirtisation specimens, which indicates that on a comparison between specimens with larger significant differences of roughness (like AB and hirtisation specimens) the fatigue has a relationship with SR. However, as discussed before, there is no clear or strong relation between the fatigue performance and SR within the same group of specimens.

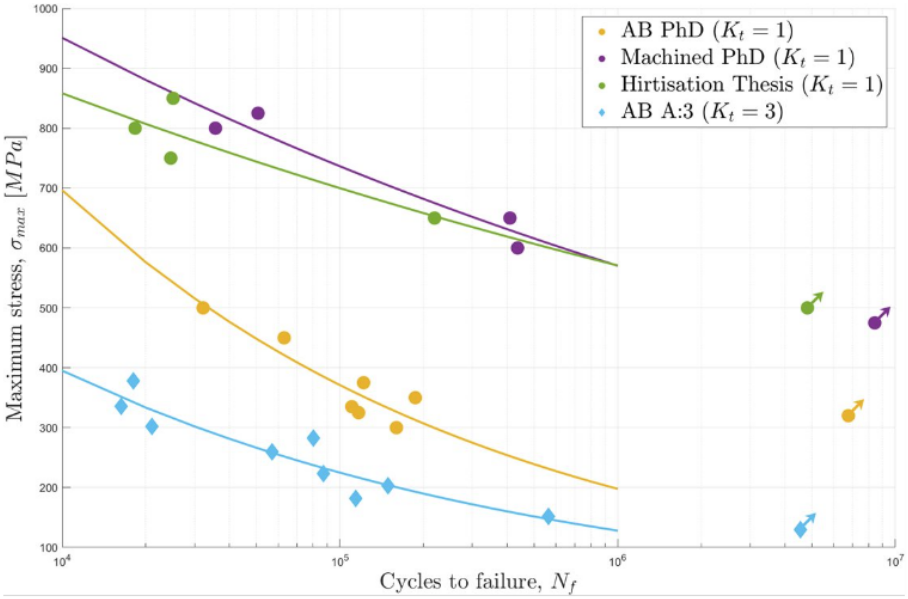

Figure 27: SN-curve for different specimens. [24] and [23]

5.3 Fracture surface characterization

The AB specimens had many crack initiation points all around the specimen, thus, no ellipse or circular shape was present on the fracture surface.
On the other hand, the AB specimens from Kahlin's PhD [23] as well as the hirtisation specimens had only one major initiation point, leading to a elliptical shape of the fatigue crack.

In Figure 28, it can be seen that the crack on the Hirt. specimens grew evenly when it comes to the depth and the span of it as the value is around the unit. It is also the case for the AB specimens analysed with this method, however, the difference is that the crack for the AB specimens was able to grow deeper into the material as the relation a/D is around 0.5 whereas for the hirtisation specimens, are closer to 0.35.

Note that in the Figure 28, one color relates to one specific specimen, having two data points for each specimen tested. When analyzed, as two sides of the specimen remain, the operator of the characterization app must get the values as close as possible, but due to the images and the micrometer values a difference is expected.

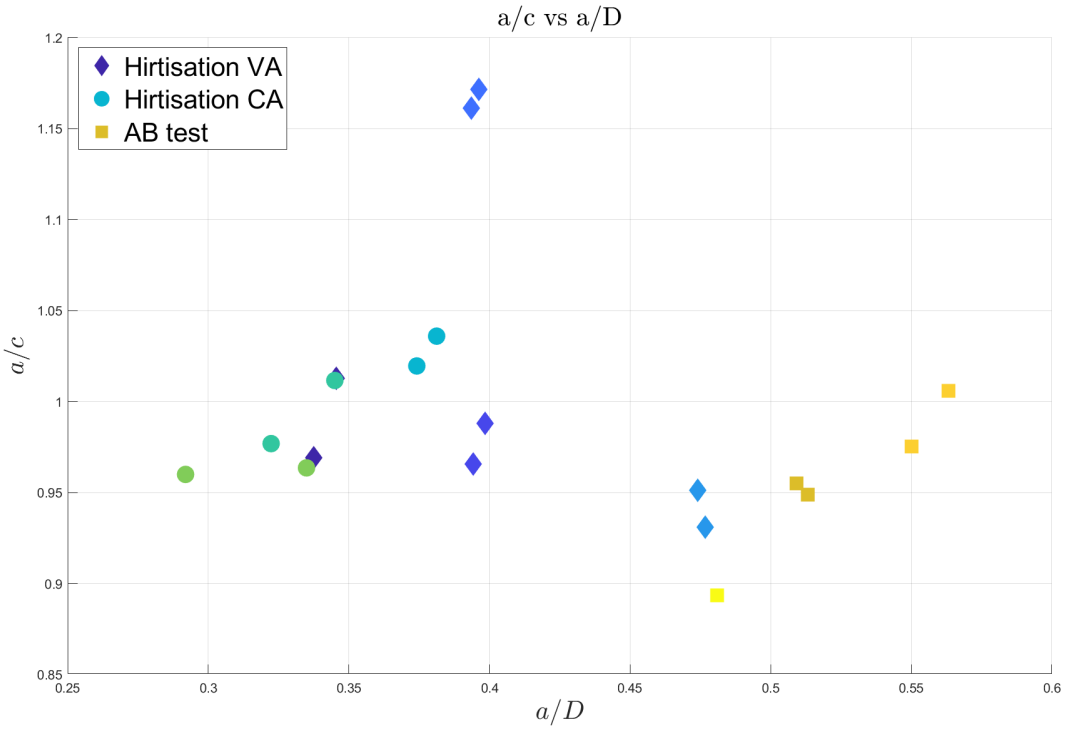

Figure 28: Characterization of fracture surface of hirtisation and 3 AB specimens.

5.4 Tensile test

Figure 29 and Figure 30 show the tensile stress-strain curve for AB-specimens. Note that the first figure ends at 2% strain as it was when the extensometer was removed.

All three tests give similar results except for the tensile strain at failure. In Table 9, the results from the tensile tests are collected.

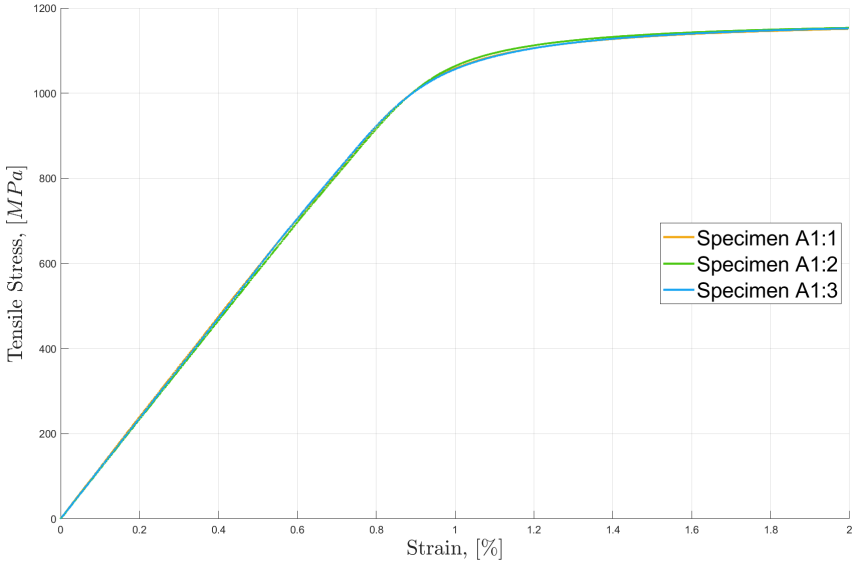

Figure 29: Tensile stress and strain from tensile tests.

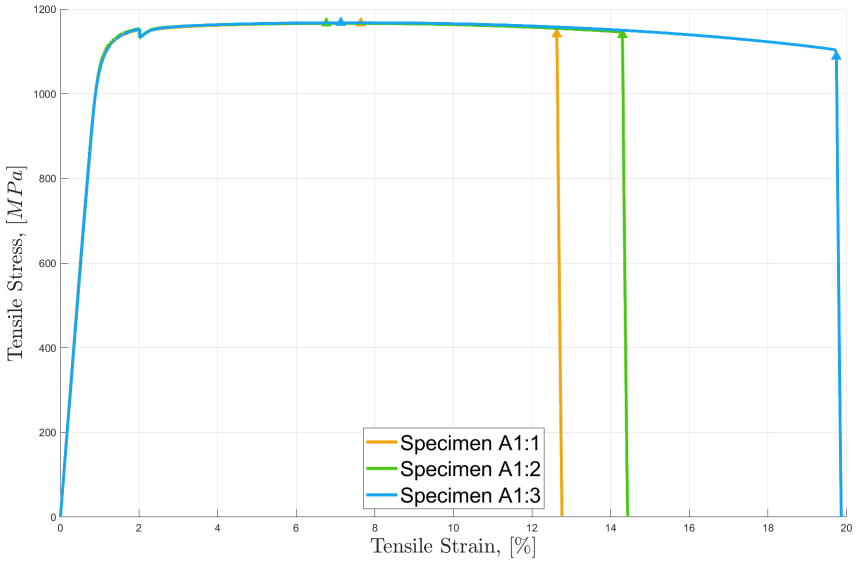

Figure 30: Tensile stress and tensile strain from tensile tests.

Parameters \Specimen	**A1:1**	**A1:2**	**A1:3**
Stress at max load [MPa]	1166.5	1166.3	1167.7
Strain at max load [%]	7.644	6.766	7.134
Elastic Modulus [GPa]	114.18	114.22	115.49
Strain at Yield (offset 0,2%) [%]	1.111	1.143	1.123
Stress at Yield (offset 0,2%) [MPa]	1090.1	1102.9	1091.4
Failure strain [%]	12.63	14.30	19.74
Failure stress [MPa]	1140.5	1138.9	1087.6

Table 9: Tensile strength parameter of AM Ti-6Al-4V from this study for AB specimens.

These results, serve as a benchmark for the fatigue testing. Analysing the results and comparing them to the ones obtained in [23], there is a slight increase in most of the parameters. However, these variations when comparing different builds manufactured by with different AM equipment and powder lots can be hard to characterize and something expected.

5.5 CA results, hirtisation

Test results from the constant amplitude cases of hirtisation specimen are presented in Table 10. The maximum force (F_{max}) registered by the Instron might result in a slightly higher stress than the one that it was supposed to reach. This difference is expected and not taken into account as the testing system is expected to not always adjust perfectly to the load applied. Also, notice that specimen *H2.1* was a runout for 500 MPa and was retested after with 850 MPa

ID	**R**	σ_{max} $[MPa]$	N_f	F_{max} $[kN]$	F_{min} $[kN]$	**Radius [mm]**
H1.1	0.1	800	18306	22.71	-1.18	6.00
H1	0.1	750	24606	21.31	-1.06	6.00
H6	0.1	650	219143	18.68	-0.31	6.03
H2.1	0.1	500	4818552	14.35	-2.11	6.02
H2.1	0.1	850	25096	24.29	-1.41	6.02

Table 10: Test results for CA testing with hirtisation specimens.

From [47], CA results were imported so that the results could be compared with more data samples. The data, represented in Figure 31, has tests performed to hirtisated specimens with a 1 and 2 step process (steps in the post-processing) as well as as-built and machined specimens. For the hirtisated specimens for Kahlin's research, the same material was used so the comparison is reasonable to make.

The results obtained in the fatigue test for the constant amplitude cases from Table 5, lay on the graph leaning more towards the machined specimens from [25] than to the hirtisation results, were results lay slightly lower.

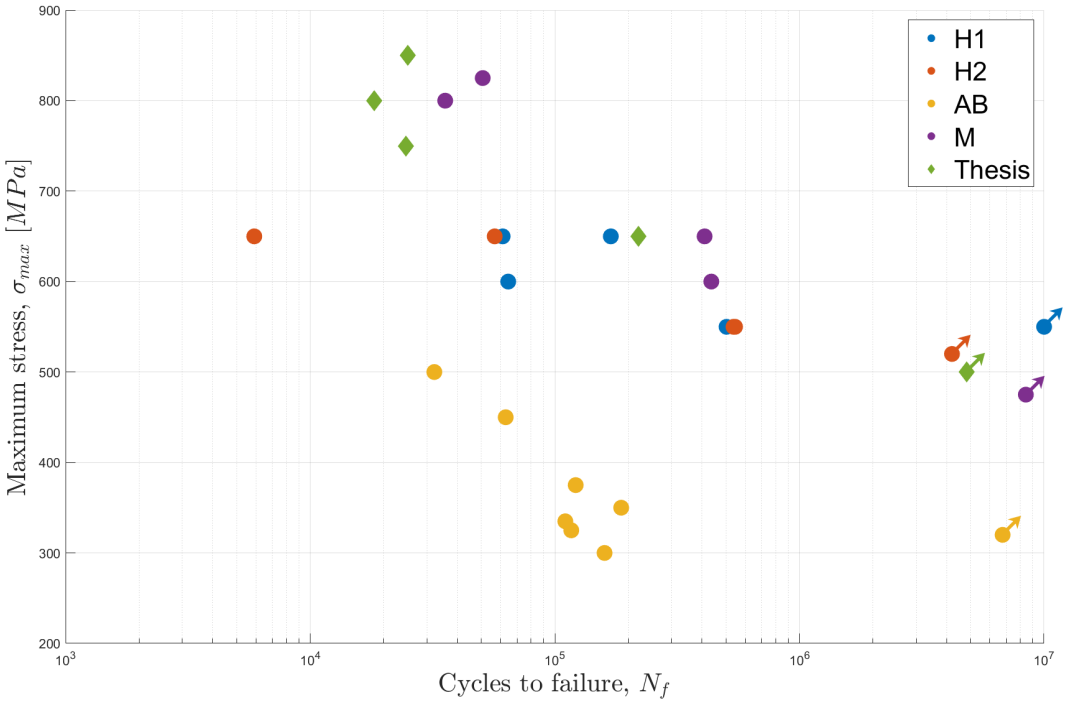

Figure 31: CA results for different stress levels and treatments with data from [23].

5.6 VA results, hirtisation

Test results from the variable amplitude tests with hirtisation specimen are presented in Table 11. Notice, that specimen *H4* was a runout for 691 MPa and was retested at 836 MPa. The condition for a runout for the variable amplitude test was set to 50000 flights, as in the industry, components are normally inspected, fixed or replaced well before such number of flights is reached.

Notice that while the objective maximum load for the test was 910 and 670 MPa, there was significant overshooting of the load as the PID set in the Instron machine has trouble to follow the set spectrum. Initial guesses had to be made as checking the maximum load was not possible when starting the test and that is why, the first test ($H7$) had significant overshooting compared to the ($H3$) as it is the last one. Same happened for $H4$ and $H4_{retest}$.

ID	σ_{max} $[MPa]$	Time [s]	N_f	F_{max} $[kN]$	F_{min} $[kN]$	$Radius$ $[mm]$
H7	955	52767	5859	27.18	-6.94	6.02
H5	893	106611	11838	25.43	-6.46	6.02
H3	924	95871	10645	26.31	-6.76	6.02
H4	691	450300	50000	19.68	-5.07	6.02
H4 retest	836	152944	16982	23.91	-6.11	6.02

Table 11: Test results for constant amplitude testing with hirtisation specimens.

5.6.1 VA life assessment

In the present section, the Palmgren and Miner rule is used to assess the test results from VA.

The constant amplitude data from Figure 31, was curve fitted was approached to the following equation:

$$\sigma_{max} = C \cdot N^{-m} \cdot (1 - R)^n \tag{5}$$

Where C and m are two constants representing the y-intercept and slope of the first section of the curve. The second part of the equation $(1 - R)^n$ is introduced in order to be able to adjust the equation to any stress ratio; where R is the specific stress ratio of the cycle and n is an exponent determined by the user to quantify the extent of how much R affects the equation. This last parameter was determined using the tests results from VA adapting it to them.

The Short-FALSTAFF spectrum has a broad spectrum of cycles with multiple stress ratios, so characterizing n is not an easy task and results could be biased on our number of flights obtained and good predictions could be simply a fluke. Nevertheless, the approach could be useful if more data was available.

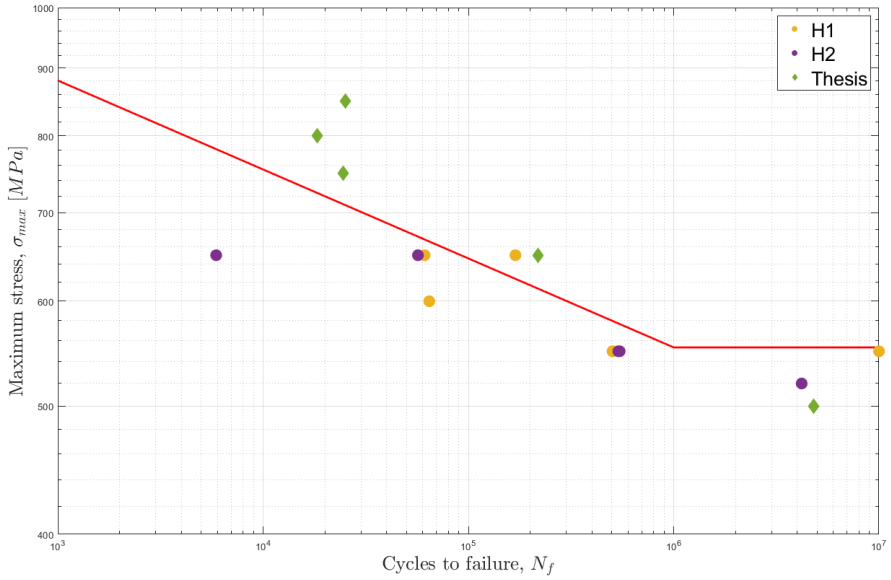

Figure 32: SN-curve curve fitted to data with $R = 0.1$.

The equation obtained after curve fitting results in constants $C = 1435.3\ MPa$ and $m = 0.0672$, note also that it was considered that after 10^6 cycles, life of the specimens would be infinite so the curve is thus, divided into two sections.

Such curve, however, is for the case of the CA amplitude data where $R = 0.1$, so an iterative process had to be made during the curve fitting and the prediction of number of flights in order to obtain proper results.

For the loop and to properly characterize a value for the parameter n, the number of flights resulting from applying the spectrum was considered. So, for a given value of n, first, curve fitting was made, then, the number of flights for the applied

load was calculated and if needed n was modified to align with the results obtained in this thesis work for the VA testing.
To calculate the number of flights for the given curve fitted equation, one first needs to calculate the number of cycles to failure for the given stress ratio. For that, R and σ were introduced in Equation 5 and thus, N_f was obtained.
With N_f for each specific cycle and the number of cycles applied obtained from the Rainflow cycle count, the Palmgren and Miner cumulative damage approach could be applied.
From Table 11, the average number of flights for the first three tests is of 9447 flights. Going over the approach mentioned before, a value of n was determined to $n = 0.226$ resulting in a number of flights of 11039. Which is close to the number obtained as an average.
If with such equation and value of n, the fatigue life prediction was made for the 670 MPa, runout results are obtained.
Validation of this method is tricky as mentioned, not a lot of data is available; however, $H4$ was retested at 836 MPa stress level obtaining 16982 flights.
When the same prediction is done for such loading scenario, the predicted amount of flights is of 38739 flights. Thus, there is a significant difference between the retest result and the predicted value.

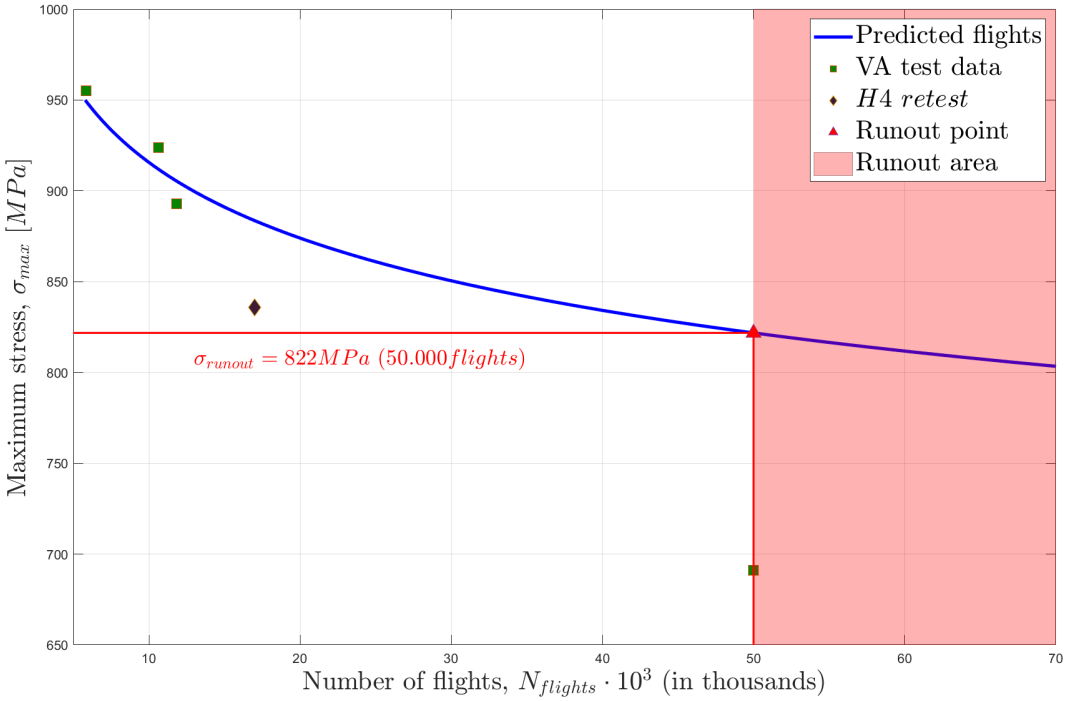

Figure 33: Number of flights prediction from VA data for hirtisation specimens.

Plotting the expected number of flights from the model obtained against the data from the fatigue test in Figure 33, it can be observed that the test data falls well in the model initially as it was assessed to it, however, little data was available, and thus, this model of assessment of number of flights could be improved further as the

retest showed significant difference. Apart from improving the model, this difference could also be due to the specimen been tested already at 691 MPa, which from the cumulative damage approach, it will have affected the life of the specimen as some of the cycles will be above the Goodman line. From the graph and the condition of considering runouts at 50.000 $flights$, the stress at which runouts should be expected is of $\sigma_{max} = 822\ MPa$, this however, does not mean that if the test were to keep running, the specimen would not fail.

5.7 CA test results, As-Built

The test results from the constant amplitude cases of the as-built specimens are attached in subsection A.1 due to the large amount of data. Note that all specimens have a minimum radius of 6.5 mm, so only the maximum and minimum stress is given and not the force. Also, note that the stress ratios do not perfectly correspond to the objective for each specimen; however, as mentioned in the hirtisation results, it is due to an over or undershooting of the hydraulic system, but the difference is insignificant so the test data can be taken as valid.

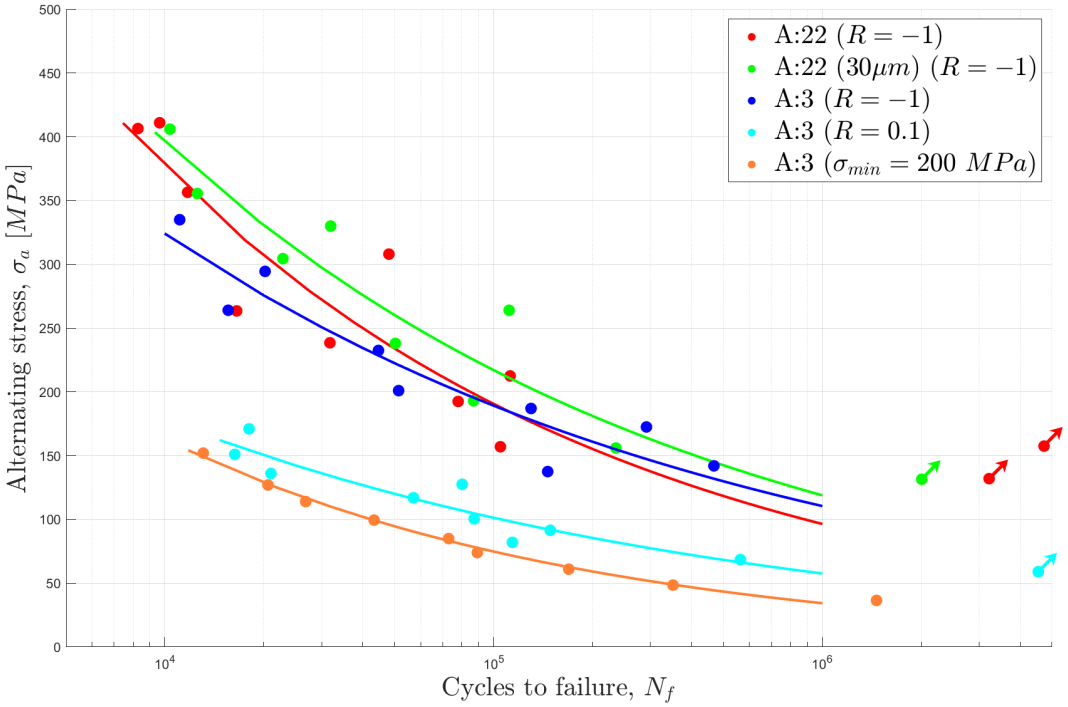

Figure 34: CA results for all AB result with curve fitting.

In Figure 34, the test results for all as-built specimens are shown as well as their log-linear fit line. For each specimen type; $A2.2$, $A2.2(30\mu m)$, $A3(-1)$, $A3(0.1)$ and $A3(200)$, curve fitting has been applied with the same equation as for the life prediction model but eliminating the stress ratio part, resulting in:

$$\sigma = C \cdot N^{-m} \tag{6}$$

5.7.1 Strain measurements AB

Figure 35 shows the measured max and min strains for $A3$ specimens.

In the figure, the results above 0% indicate the maximum of the strain tracking measurement while the plotted lines below 0% indicate the minimum strain tracked measurement.
When setting up the extensometer, it was challenging to get to 0% as there was no reset button, so all curves have been shifted to have the average of both measurements at 0 on the first data logged, this way offsets on the later data recorded are not modified.

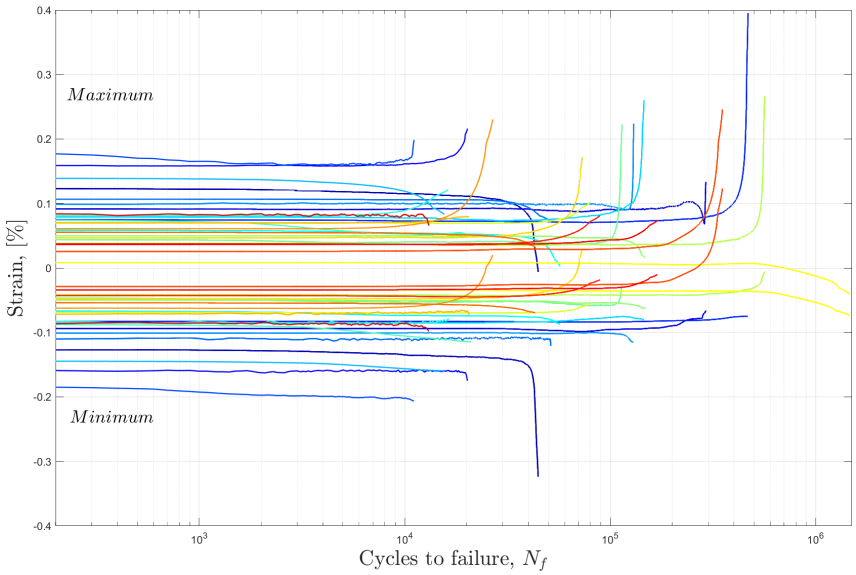

Figure 35: Maximum (above 0%) and minimum (below 0%) strain against cycles to failure for $A:3$ specimens.

All measurements remain fairly constant although a logarithmic scale has been applied. There are some specimens that could potentially exhibit cyclic hardening and the maximum and minimum tend to drop in value. This phenomenon however, is more noticeable to the specimens tested at higher loads resulting in lower fatigue life. At the final stage, the crack however seem to grow rapidly reaching failure.

If however, the range is plotted, it can be seen that there is no significant difference or trend in the results, and thus, the potential hardening cannot be confirmed. If the hysteresis loops were recorded, one could identify such effect properly, however, due to the excessive amount of data, it was unable to do so.

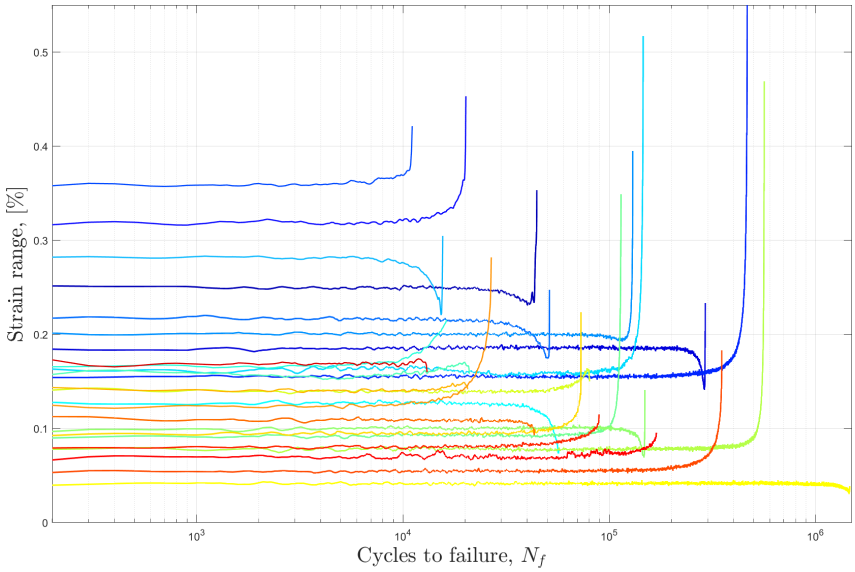

Figure 36: Strain range against cycles to failure for $A:3$ specimens.

5.8 Surface roughness and Kt effect on fatigue

Fatigue tests results from the previous cases have been used to evaluate the effect of different surface roughness conditions on the fatigue life of the specimens. The evaluation, has been carried out for the specimens tested with a stress ratio of $R = -1$; being the first three cases from Figure 34. If such cases are plotted again in Figure 37, it can be seen more clearly that no remarkable effect of surface roughness on the fatigue life of the specimens is appreciated. The only difference between the curves, could potentially be due to the fatigue scatter or due to the roughness of each of the specimens, so it cannot be confirmed any theory with certainty. The only noticeable difference is for the $A:3(-1)$, is that the slope for such cases is lower than for the $A:2.2$. But still, this now could come from the difference in K_t in the specimens and not the surface roughness of each batch as the show similar parameters.

It must be remarked, as seen in subsection 5.1, that not a significant different in the SR parameters from batches is seen, as thus, not a big comparison can be made from the experimental results.

With the surface roughness parameters from subsection 5.1, a color map plot with the as-built test results can be made as seen in paper [48]. In Figure 38 the same data was used as in Figure 37, where specimens with different K_t but same stress ratio ($R = -1$) are plotted. In Figure 39 however, only the $A:22$ specimens are plotted meaning same K_t and same R. While more plots could be made with the different SR parameters measured or a combination of them, no relation between the SR and the fatigue life can be observed. In [48], however, a significant relation was detected so for the data in this thesis, it could be due to a lower difference in the SR or the difference in the measurements, as in the mentioned paper, CT scans

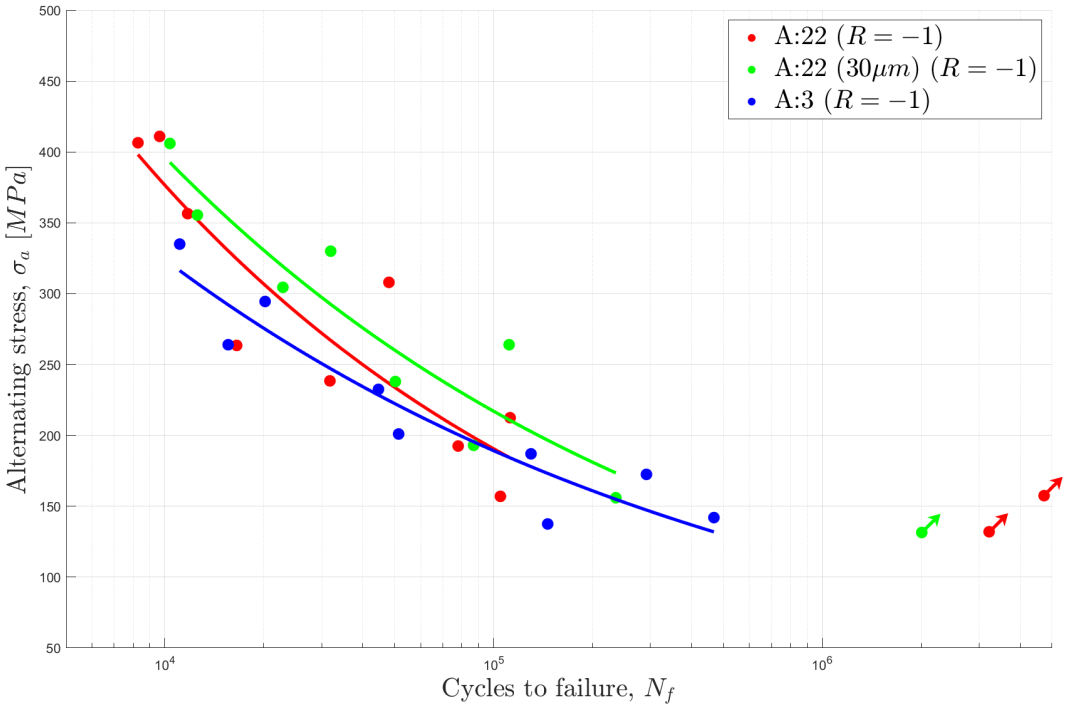

Figure 37: Surface roughness effects on the S-N curve of Ti-6Al-4V with a stress ratio of $R = -1$.

were also performed whereas in this project, only profile measurements were taken.

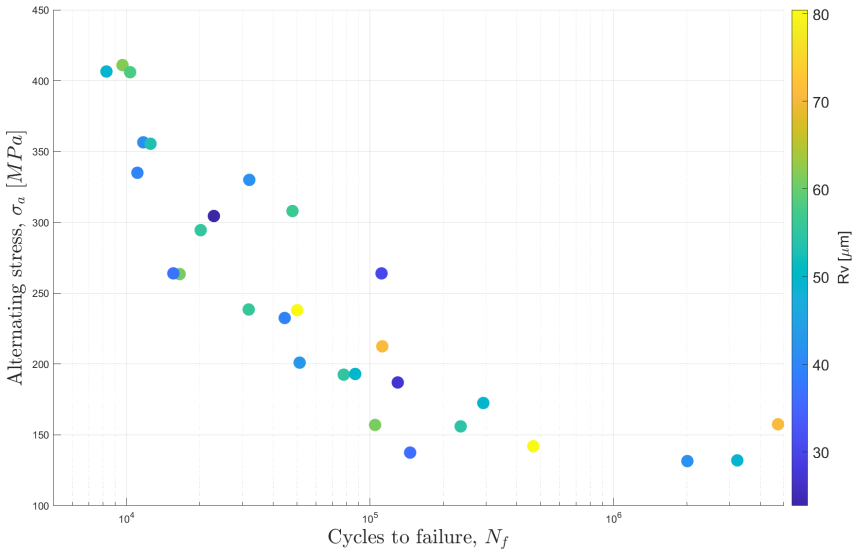

Figure 38: AB test data with R_v parameter for $A:22$ and $A3$ specimens for $R = -1$.

:

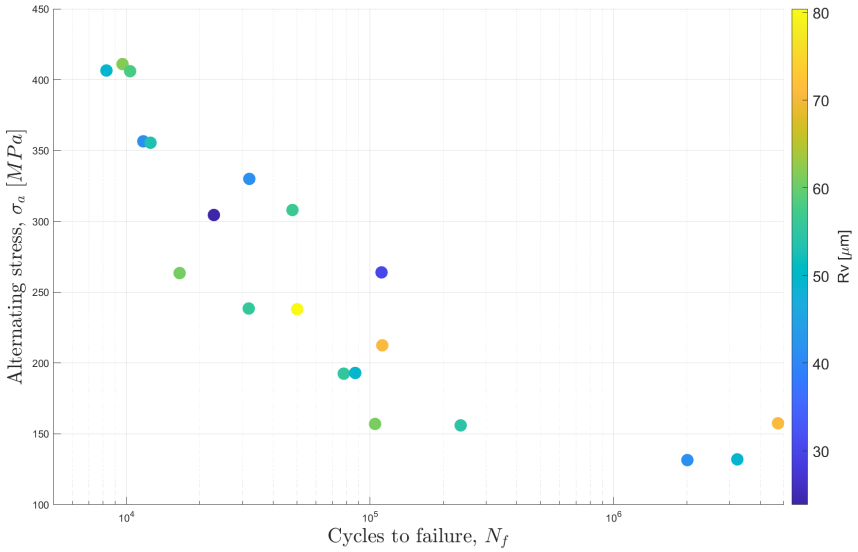

Figure 39: AB test data with R_v parameter for $A:22$ specimens ($K_t = 2.2$) and $R = -1$.

:

In Figure 27 from subsection 5.2, when comparing the notched as-built specimens from our thesis with a K_t of 3 to un-notched as-built specimens with a K_t of 1 from [24], a noticeable but smaller impact on fatigue life compared to the surface condition was observed. However, this comparison might be unfair as both groups of specimens were printed by two different the manufacturers.

5.9 Impact of layer thickness

To assess the effect of layer thickness on surface roughness and fatigue life, two groups of specimens with different layer thickness were compared to each other. From Figure 41, the Peak Height parameter (R_p)of A2.30 has a higher variance (248.19) compared to the one of A22.60 (45.95), indicating more variability in R_p values for the 30 micrometer layer. Also, Valley Depth parameter (R_v)of A2.30 has a variance of 274.35 while A22.60 has a variance of 69.21. This again shows more variability for the 30 micrometer layer.

Also, Figure 40 illustrates comparison between the average value of the surface roughness parameters of A2 specimens which were built with layer thickness of 60 micrometer and A2.30 specimens that were built with layer thickness of 30 micrometer. It shows that A2.60 specimens have a little higher surface roughness compared to A2 .30. This makes sense as the larger layer height produces more steps between layers, leading to a higher surface roughness. Theoretically, this thicker layer might lead to lower fatigue life as it can act as stress concentrators and initiation sites for cracks. To compare the data of the two groups statistically, linear regression was done as shown in Figure 42. The analysis of covariance indicates that the two groups do not differ significantly in terms of slopes and intercepts. However, this conclusion can not be verified 100% as the data are not enough to prove the relation between layer thickness and fatigue life. This could also be seen in the previous Figure 37, where the prediction intervals overlap each other and thus, the opposite

results could have been obtained.

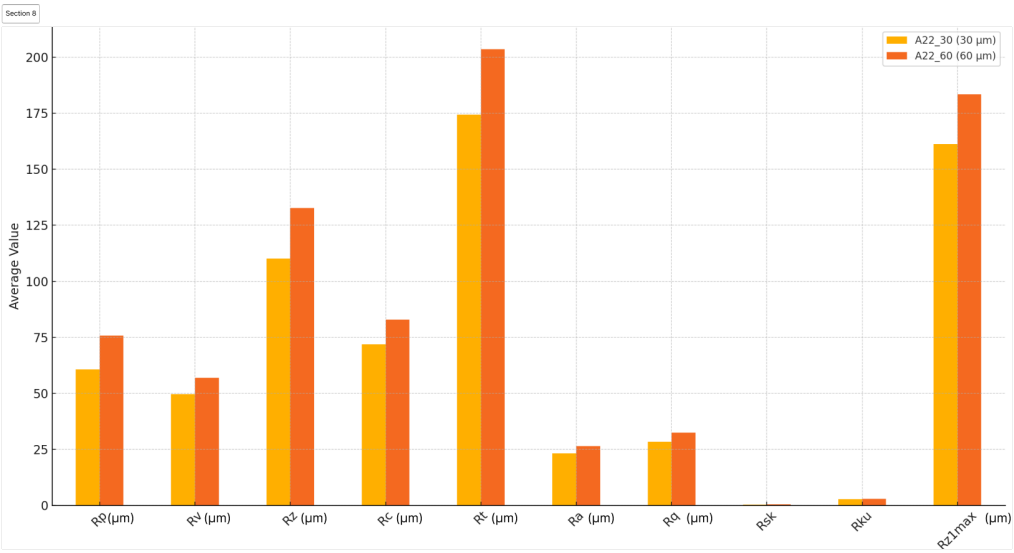

Figure 40: Comparison of the surface roughness parameters for the A2.30 and A2.60

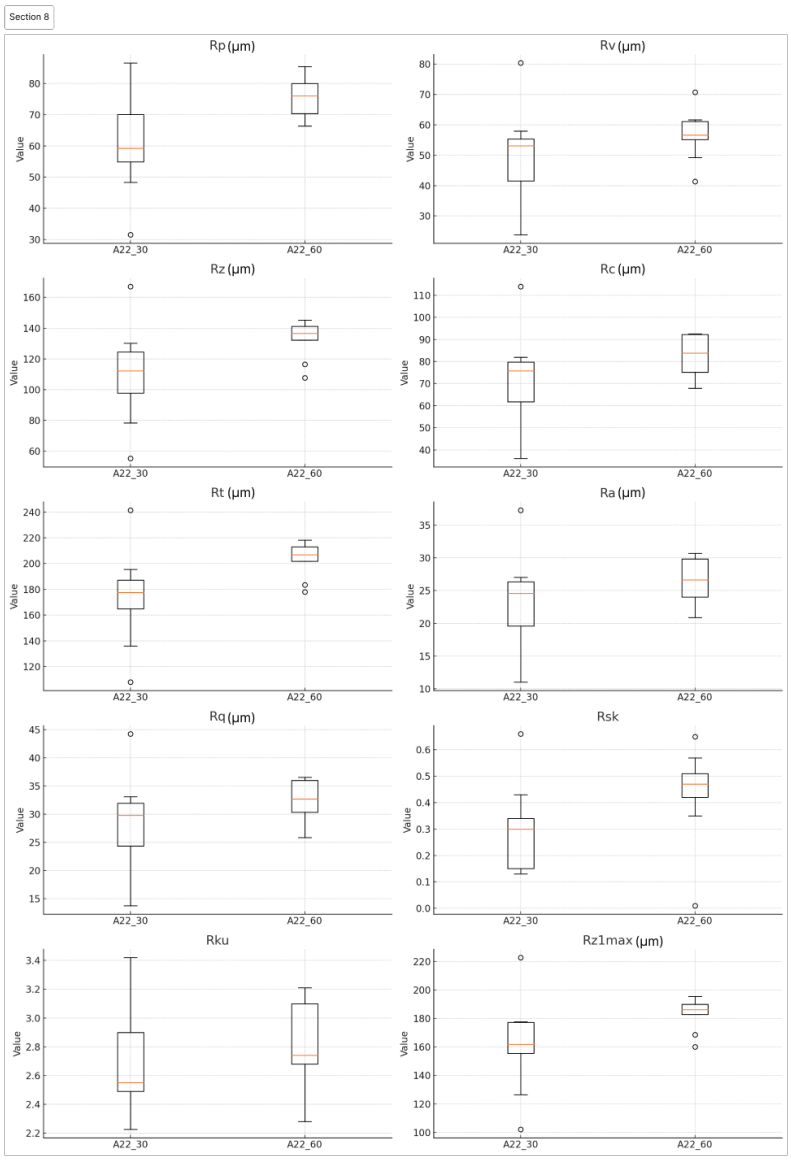

Figure 41: Bar charts illustrates the average values for each surface roughness parameter

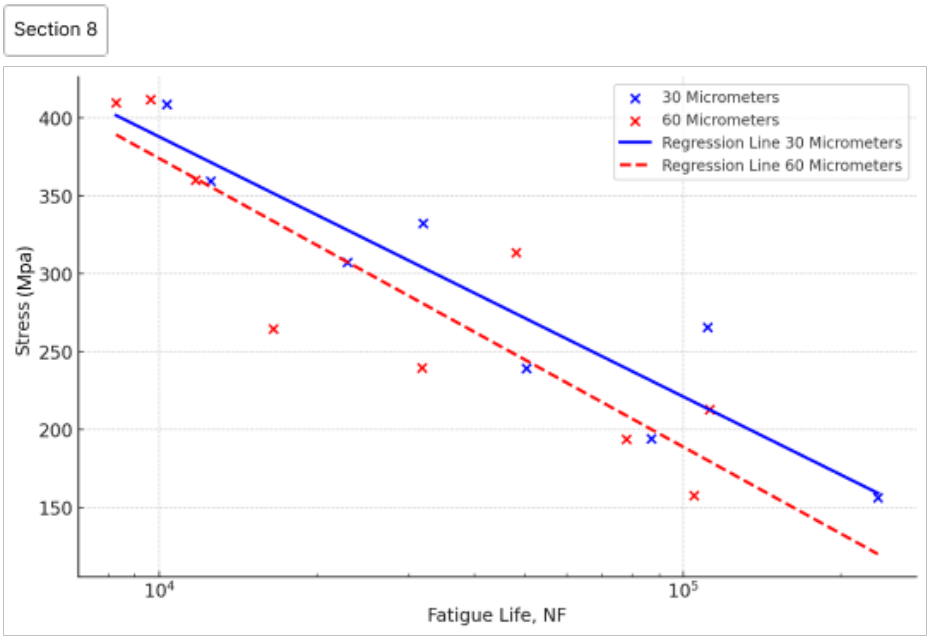

Figure 42: Regression Comparison of Stress Vs Fatigue Life of A2.30 and A2.60

5.10 Notch characteristics

Figure 44 demonstrates the notch shape which shows that there are three parts of the notch; rough part, middle part, and smooth part. The difference in roughness between the top part and the middle part is a result of being with or oppose to the building direction as each layer is deposited by the laser in a layer-by-layer fashion from bottom to top. Figure 45b, Figure 45a, Figure 45c, and Figure 45d show how the surface roughness parameters differ between the rough section of the notch and the middle section.

Theoretically, when the specimen breaks, it is expected that this breakage will occur exactly in the middle of the notch as it is the smallest geometry which will be a concentration point for the stress [49]. However, after the test, it was noticed that the fracture in all the specimens almost happens in the top part(the rougher part) of the notch, not in the middle part as shown is Figure 43. This observation indicates that the roughness is an important factor for fatigue point of view.

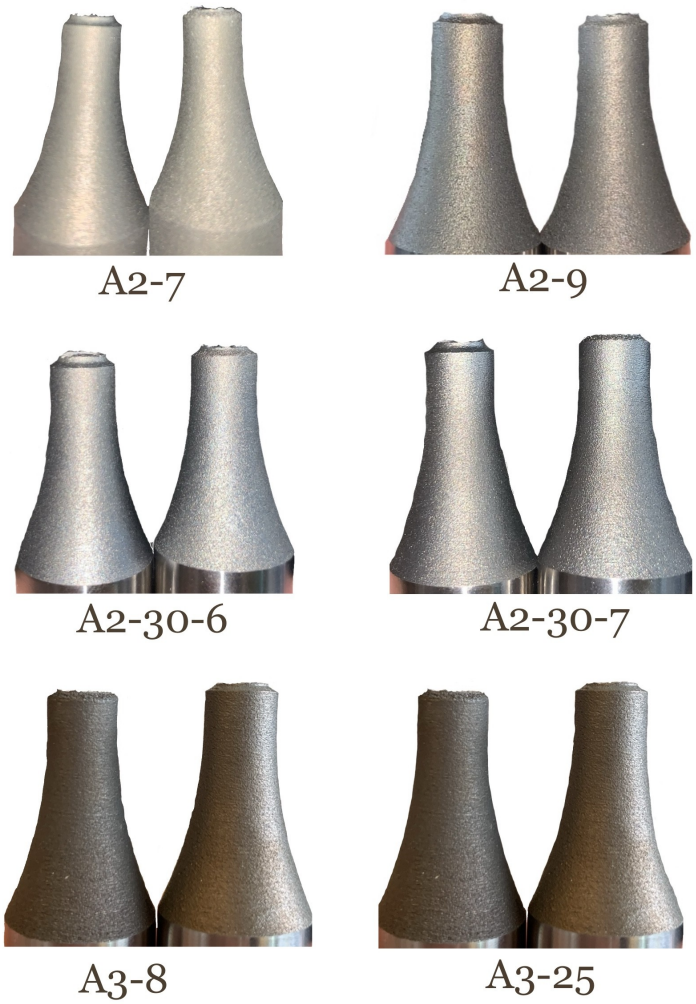

Figure 43: The breakage demonstration of different Specimens

Moreover,during analysing the notch fracture, there is a noticeable trend where the values for the rough section and the middle section appear to follow similar patterns for A3 specimens. It appears that when there is an increase or decrease in the rough section's surface roughness parameters, there is a corresponding increase or decrease in the middle section's parameters as well. There was suspicion that the methodology used in SEM for measuring ST might introduce a systematic error. However, the measurements were controlled and done in the exact same conditions. Thus, if the method has a certain sensitivity or error, it could reflect similarly in both sections. Possible explanation for this behavior is that the manufacturing process might be consistent across the entire specimen, means that the variations affecting one part might similarly affect the other parts due to the uniform application of the printing. Another reason is that the measurements were taken across the layers of the specimen (horizontally). This means that each measurement is representing only the layers which indicates that the roughness measurements in the rough and middle sections of the same layer would naturally follow similar trends. To answer this question or explain the trend better, more future investigations need to be done

by measuring different profile for the same notch from all around the specimen to see if the behaviour is the same on each side of the notch or not. Also the method needs to be verified more.

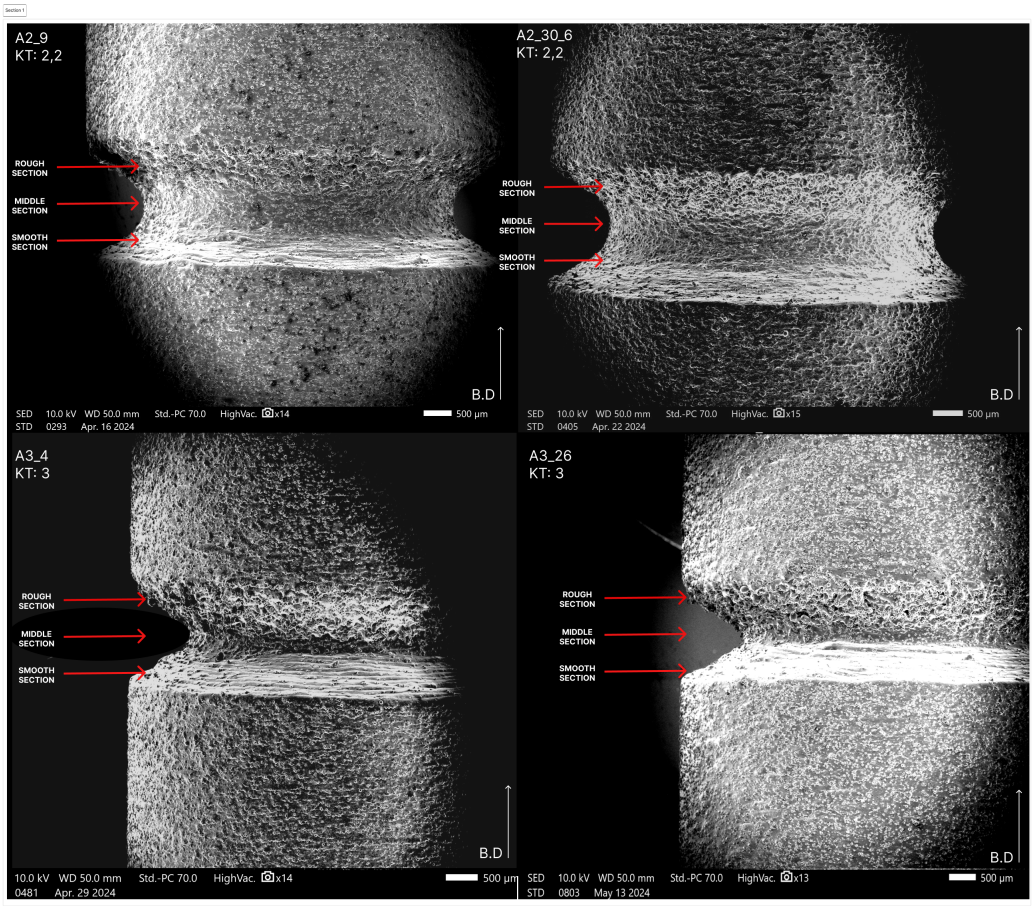

Figure 44: The notch demonstrations for different Specimens

(a) Rp(µm) values for the rough and middle sections

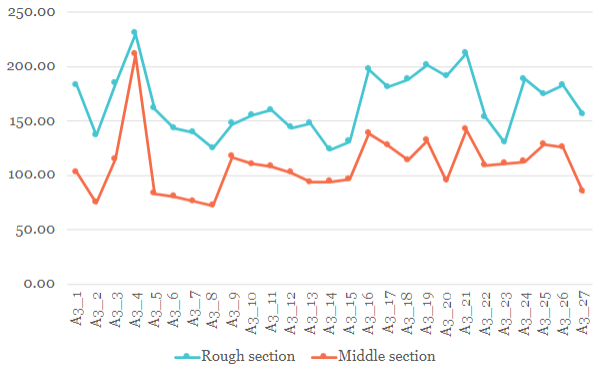

(b) Rv(µm) values for the rough and middle sections

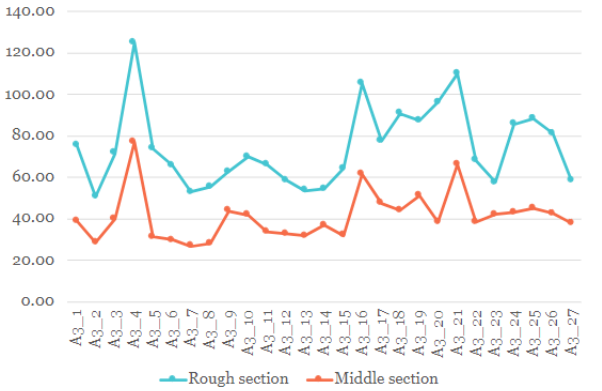

(c) Rz(µm) values for the rough and middle sections

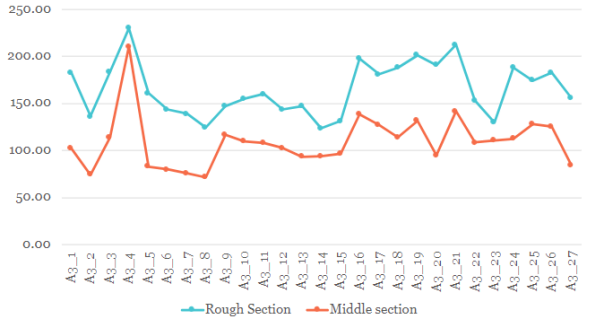

(d) Rq(µm) values for the rough and middle sections

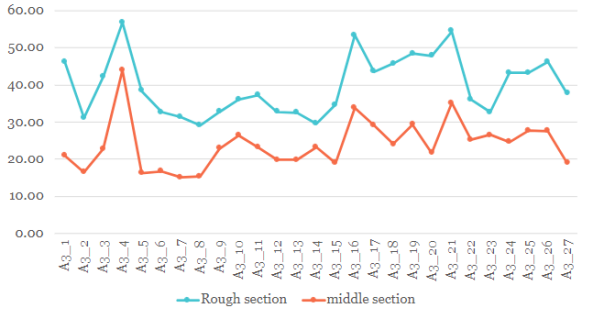

Figure 45: comparison between Surface Roughness parameters between the rough and middle sections

6 Discussion

This chapter discusses the results and answer the research questions after the specimens were tested under constant and variable amplitude loading, both in their as-built condition and after undergoing hirtisation treatment. It also considers the limitations and future recommendations for this study.

6.1 Characterization of the surface roughness of AM parts to assess its impact on fatigue life

The characterization of surface roughness was done effectively. After measuring the roughness of all specimens (both the AB and the hirtisation ones) using the stylus profilometer for hirtisation-treated specimens and the scanning electron microscope SEM for as-built specimens the relevant parameters to the study (Rq, Rv, Rp, Rz, Rsk and Rku) were utilized to quantify surface roughness. The surface roughness for each specimen was compared to the fatigue life cycles. The results from subsection 5.8 showed that there is no observed correlation between surface roughness and fatigue life of the specimens of the same group which disagrees with the findings of other studies that validates the relation between surface roughness and fatigue life. The study also demonstrated that hirtisation treatment effectively reduces surface roughness parameters by 75-80%. This reduction in surface roughness enhances the fatigue performance of the specimens. Which demonstrated an increase in fatigue life which also increases the reliability of components to be used in aerospace applications.
Another aspect investigated in this study is the evaluation of the effect of layer thickness on surface roughness and fatigue life by comparing two groups of specimens with different layer thicknesses. Surface roughness parameters Rp and Rv were assessed, and their variances were analyzed to understand the variability in surface roughness for each layer thickness. While the surface roughness parameters showed higher variability for the smoother layer thickness specimens, the overall surface roughness was slightly higher for the rough layer specimens. The expected correlation between thicker layers and reduced fatigue life was not strongly supported by the available data.

6.2 The influence of the combined factors of surface roughness and geometrical stress concentrations on the fatigue behaviour

The combined factors of surface roughness and geometrical stress concentrations significantly influence the fatigue behavior of AM components. Surface roughness introduces micro-scale stress concentrators, while geometric features such as notches

create macro-scale stress concentrations. When these factors coexist, they increase the stress at specific locations, accelerating crack initiation and propagation. Not enough investigation was done to test and compare notched as-built specimens to un-notched as-built specimens, however, comparing the results in this study to the un-notched as-built specimens that were tested under almost the same load from [24], there is an observation that specimens with notches have lower fatigue life compared to the un-notched ones. In addition to that, the specimens were not tested under the same load, only three were tested with almost the same maximum stress which is not enough data to make a theory from.
Investigating the notch shape in specimens, it is characterized by three distinct parts: the rough part, the middle part, and the smooth part. The difference in roughness between the rough part and the middle part is attributed to the direction in which the specimen is built. Not only that, but also the roughness of different parts of the notch contributed to where the fracture will happen. It was noticed that breakage occurred in the rough part of the notch rather than the middle part which contrary to theoretical expectations. This observation indicates that the surface roughness of the notch plays a significant role in fatigue life.

During the observation of notch surface and fracture of A3 specimens, an interesting trend were observed in the analysis the surface roughness parameters for the rough and middle sections of the notch. It seems that both sections tend to follow similar patterns. When there is an increase or decrease in the rough section's surface roughness, the middle section's parameters show a corresponding change. This observed trend is not fully studied or understood, so further investigations are necessary.

6.3 The fatigue behaviour of hirtisation specimens under both constant and variable amplitude loading

The fatigue behavior of hirtisation specimens shows consistency under both constant and variable amplitude loading conditions, although some variations were observed. Under constant amplitude loading, hirtisation specimens consistently showed improved fatigue life compared to as-built and machined specimens, as the smoother surface roughness reduces the stress concentrations. It would have been an advantage if we could compare this hirtisation specimens to the as built specimens, but there is a combined factor which is the notches in the as-built specimens that made this comparison unfair to make.Under variable amplitude loading, the fatigue life prediction using the Palmgren and Miner rule showed somewhat reasonable results. It predicted number of flights generally aligned with test data initially but diverged with further testing. The model could be improved with more data.

6.4 The characteristics of the fatigue initiation point(s) in AM material

An observation of fracture surface was done for both hirtisation and AB specimens using stereo microscope. For the hirtisation specimens, most of them have surface fracture and only one specimen has internal fracture. This clear behaviour of fracture made it possible to characteristics the fatigue initiation points for this specimen. Using a developed MATLAB GUI to characterize the fracture surfaces of specimens, it was observed that the cracks in hirtisation specimens grew evenly in depth and span, with values close to unity. In contrast, AB specimens showed deeper crack growth into the material but overall they were hard to identify using this method due to their multiple crack initiation points.

6.5 The relation between irregularities at initiation points and fatigue life

The shape and size of irregularities at fatigue initiation points can be somehow related to the fatigue life of AM components. Most of the hirtisation specimens have surface fracture as a result from larger and deep valleys in the surface that create higher stress concentrations at these points hence facilitate quicker crack initiation and growth. Thereby, the micro-stress concentrators reduce the fatigue life of the specimens. As-built specimens were examples for macro stress concentrators which are notches. For the as-built specimens the fracture happens on the notches always, moreover, as discussed in subsection 5.10 It happens at the rough section of the notch that has both the effect of Kt and SR. Hirtisation treatment was shown also to effectively reduce the size and number of these irregularities of the specimen surface, thereby enhancing its fatigue life.

6.6 Limitations and future recommendations

Based on the results and findings, several future research and study are recommended to enhance the understanding and optimization of fatigue behavior in additive manufactured Ti-6Al-4V parts. One of the biggest limitations for this study was the lack of data. Thus, it is recommended to conduct additional tests and experiments under various conditions to gather a more comprehensive data set. This will help in comparing results more effectively and validating the effect of different factors without the combined factor effects of varied experimental setups. Besides, there was no enough time to study different sections of notches which is needed to understand the trend behind the similarity of rough and middle section of the notch. This further investigation can help in understanding how surface roughness varies within notched areas and its impact on fatigue life that can also provide deeper insights into the failure mechanisms of complex geometries. The methods used for measuring surface roughness should be as well improved and validated. Besides, the VA life prediction model should be refined with more comprehensive data. Another point that was out of this study's scope is to focus on the correlation between strain measurements

during tests and crack growth. One challenge of this point is that not all the strain data were saved from the beginning of the fatigue test until the specimen breaks as there was not enough memory to save all the strain data which would contribute to better predict the growth rate of cracks. Moreover, more investigations need to be done to quantify the irregularities of the surface and the notch.The fatigue fracture surfaces, and the initiation points need to be characterized and studied. Also, do various loads and load ratios have correlation with the number of initiation points? Investigate the relationship between fatigue initiation points and the fatigue life by designing a study that focuses on the size and shape of initiation sites, and their correlation with surface roughness and other factors. Some studies recommend that there is a relation between layer thickness and the fatigue performance of the material, which was not observed in this study. Thus, more experimental data needs to be collected to prove or dis-prove the theory.

7 Conclusions

This thesis investigated the impact of surface conditions on the fatigue life of Ti-6Al-4V components produced by L-PBF, from the perspective of aerospace applications. Through extensive experiments and analysis, several key findings and answers to the research questions were made. It highlighted that surface roughness plays a significant role in the fatigue behavior of AM components but this relationship between surface roughness parameters and fatigue life that still needs to be studied. Comparing AB specimens to the treated with hirtisation- a post-processing surface treatment- it was noticed that significant improvements in reducing surface roughness by approximately 75-80%, which in turn enhanced the fatigue performance of the treated specimens. This improvement underscores the potential of surface treatments in extending the fatigue life of AM components as its fatigue performance is close the the one of the machined specimens. Moreover, the study investigated the combined effects of surface roughness and geometrical stress concentrations, such as notches, on fatigue behavior. It was found that the presence of notches reduced fatigue life, and fractures tended to initiate at the rough sections of the notches rather than at the middle, theoretically expected stress concentration points. This indicates that surface roughness within notches has a more profound impact on fatigue initiation and propagation than previously understood. A variable amplitude prediction model was done to predict the number of flights but still needs more data to validate it.

Limitations in the study, including a lack of comprehensive data and constraints in time, suggest that further research is needed to fully understand the relation between surface roughness, stress concentrations, and fatigue life. Future work should focus on expanding the data set, refining surface roughness measurement techniques, studying each parameter and its effect on fatigue life separately and exploring the microstructure contribution to the different parameters.

In conclusion, this research provides valuable insights into the fatigue behavior of AM Ti-6Al-4V parts, with findings that contribute to the understanding and optimization of additive manufacturing processes for aerospace applications.

A Appendix

A.1 Constant amplitude testing As-Built

Specimen	σ_{max} [MPa]	σ_{min} [MPa]	σ_a [MPa]	R	Nf
A2.2:1	314	-302	308	-0.96	48018
A2.2:2	265	-262	263	-0.99	16528
A2.2:3	194	-191	193	-0.99	77979
A2.2:4 (runout)	158	-157	157	-0.99	4726675
A2.2:4 (retest)	213	-212	212	-0.99	112251
A2.2:5	412	-410	411	-1.00	9634
A2.2:6	240	-237	238	-0.99	31759
A2.2:7	158	-156	157	-0.99	104843
A2.2:8 (runout)	133	-131	132	-0.98	3216799
A2.2:8 (retest)	410	-403	406	-0.98	8276
A2.2:9	360	-353	356	-0.98	11723

Table 12: Constant amplitude test result AB for specimen group A2.2.

Specimen	σ_{max} [MPa]	σ_{min} [MPa]	σ_a [MPa]	R	Nf
A2.2_30:1	308	-301	304	-0.98	22848
A2.2_30:2	266	-262	264	-0.99	111441
A2.2_30:3	194	-192	193	-0.99	86902
A2.2_30:5	156	-156	156	-1.00	235440
A2.2_30:6	409	-403	406	-0.99	10352
A2.2_30:7 (runout)	132	-131	132	-0.99	2006742
A2.2_30:7 (retest)	333	-327	330	-0.98	31932
A2.2_30:8	359	-352	356	-0.98	12550
A2.2_30:9	240	-236	238	-0.99	50227

Table 13: Constant amplitude test result AB for specimen group A2.2 with $30\mu m$ layer.

Specimen	σ_{max} [MPa]	σ_{min} [MPa]	σ_a [MPa]	R	Nf
A3:1	233	-232	233	-0.99	44619
A3:2	173	-172	172	-0.99	291645
A3:3	297	-292	294	-0.98	20168
A3:4	143	-141	142	-0.99	467825
A3:5	338	-332	335	-0.98	11087
A3:6	203	-199	201	-0.98	51391
A3:7	188	-186	187	-0.99	129932
A3:8	266	-262	264	-0.98	15575
A3:9	139	-136	138	-0.98	146023

Table 14: Constant amplitude test result AB for specimen group A3 $R = -1$.

Specimen	σ_{max} [MPa]	σ_{min} [MPa]	σ_a [MPa]	R	Nf
A3:10	260	26	117	0.10	57014
A3:11	336	34	151	0.10	16306
A3:12	302	30	136	0.10	21023
A3:13 (runout)	130	12	59	0.09	4538934
A3:13 (retest)	223	22	101	0.10	87243
A3:14	182	18	82	0.10	114048
A3:15	203	20	91	0.10	148683
A3:16	378	36	171	0.10	18021
A3:17	152	15	68	0.10	563247
A3:18	283	28	128	0.10	80211

Table 15: Constant amplitude test result AB for specimen group A3 $R = 0.1$**.**

Specimen	σ_{max} [MPa]	σ_{min} [MPa]	σ_a [MPa]	R	Nf
A3:19	273	200	37	0.73	1461869
A3:20	370	200	85	0.54	72954
A3:21	454	200	127	0.44	20576
A3:22	428	200	114	0.47	26799
A3:23	399	200	100	0.50	43273
A3:24	296	199	48	0.67	351296
A3:25	347	199	74	0.57	89181
A3:26	321	199	61	0.62	169224
A3:27	503	199	152	0.39	13079

Table 16: Constant amplitude test result AB for specimen group A3 with $\sigma_{min} = 200\ MPa$**.**

A.2 Notches pictures of A2.2 specimens

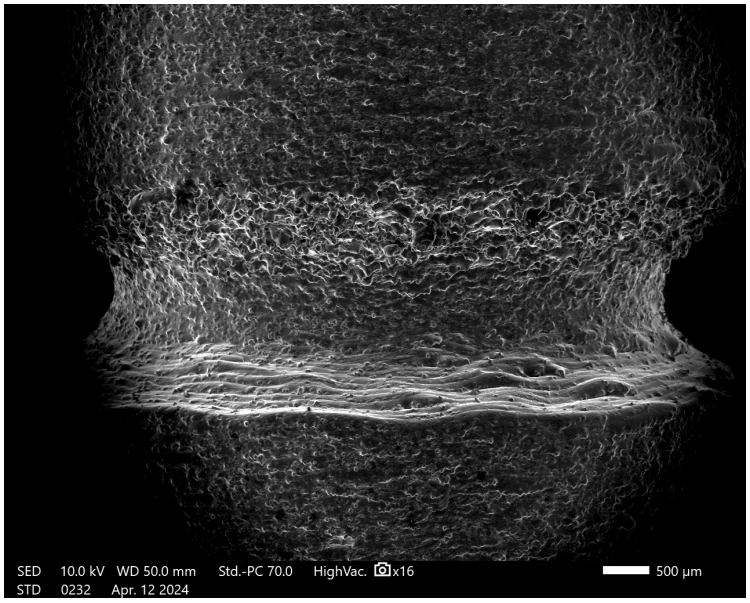

Figure 46: A2.1 Specimen

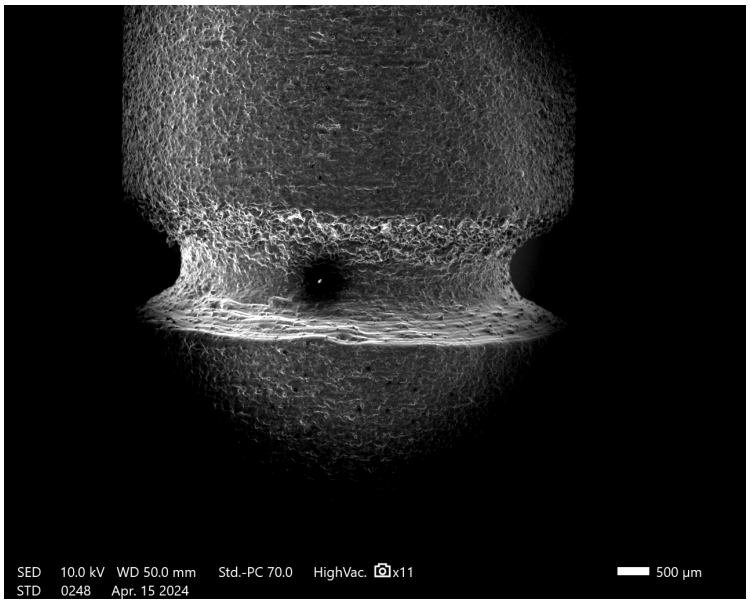

Figure 47: A2.3 Specimen

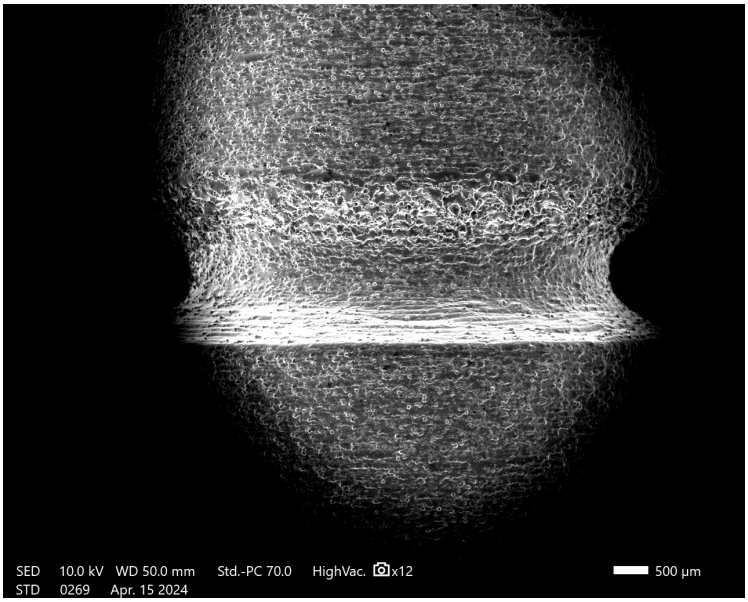

Figure 48: A2.5 Specimen

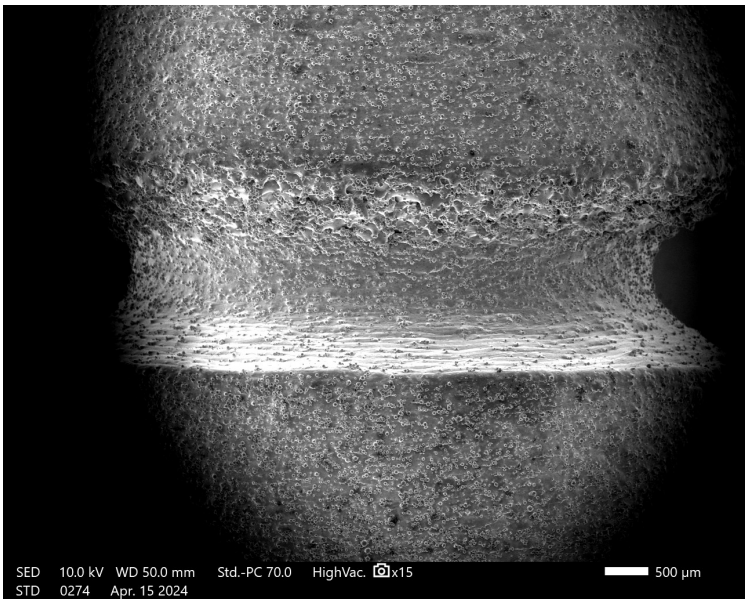

Figure 49: A2.6 Specimen

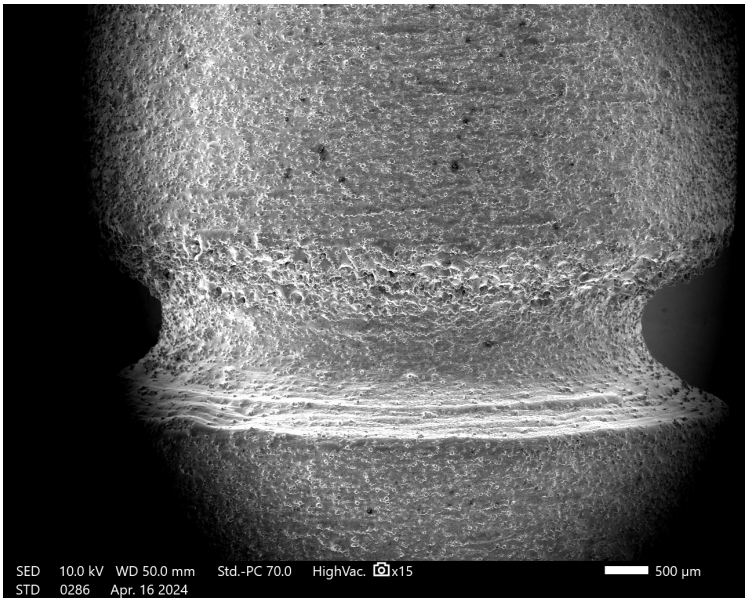

Figure 50: A2.8 Specimen

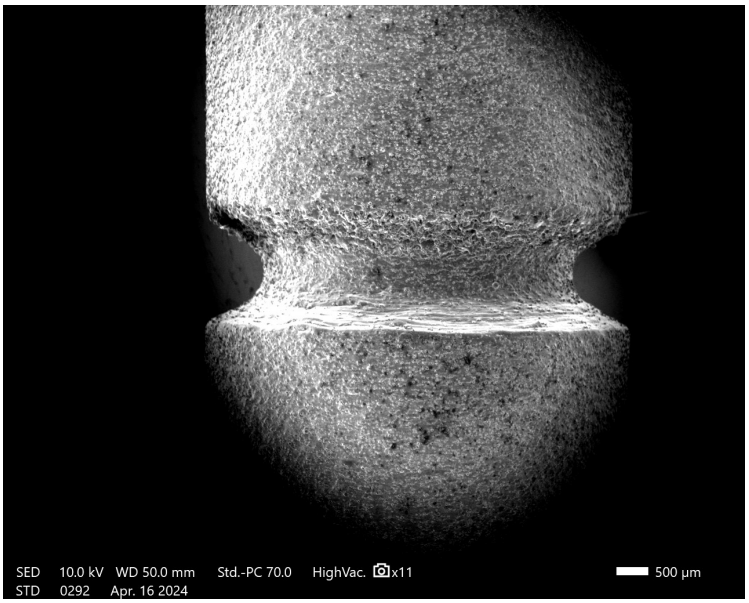

Figure 51: A2.9 Specimen

A.3 Notches pictures of A2.2 (30) specimens

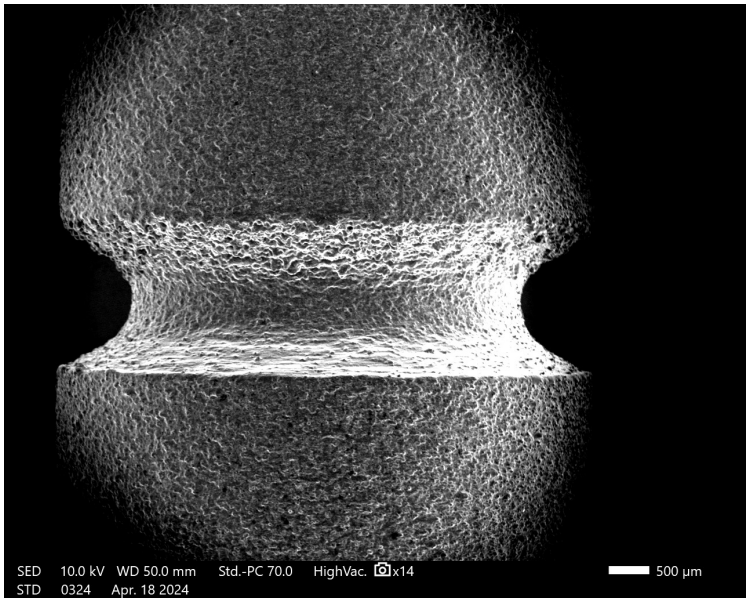

Figure 52: A2.30.1 Specimen

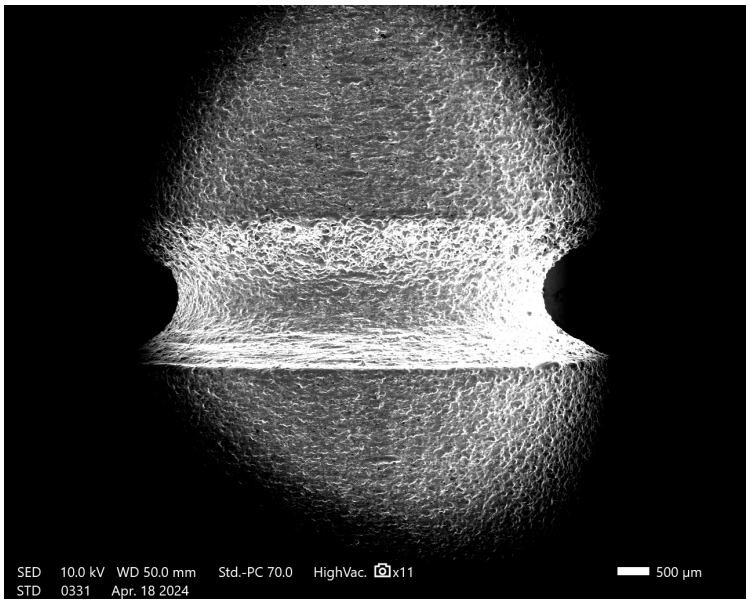

Figure 53: A2.30.2 Specimen

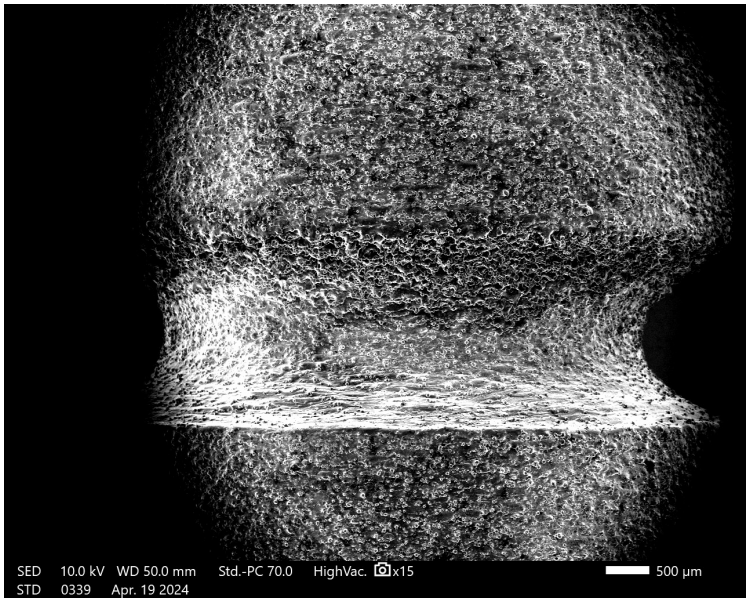

Figure 54: A2.30.3 Specimen

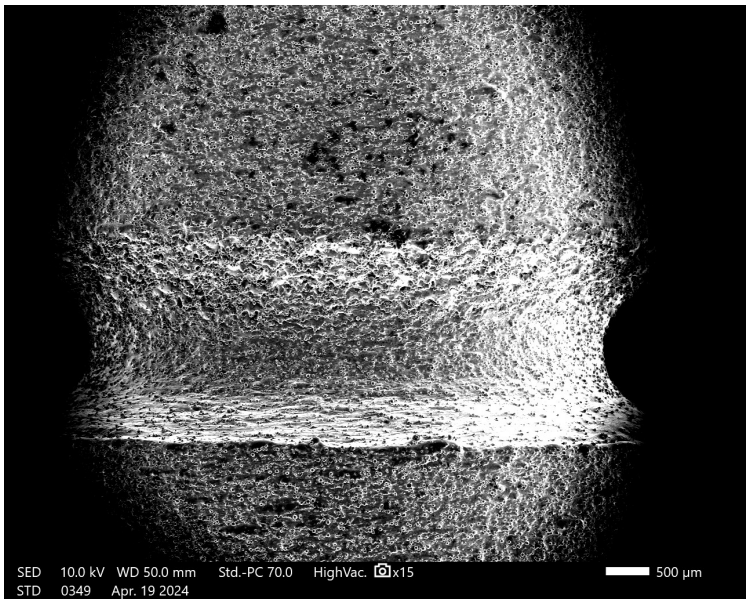

Figure 55: A2.30.4 Specimen

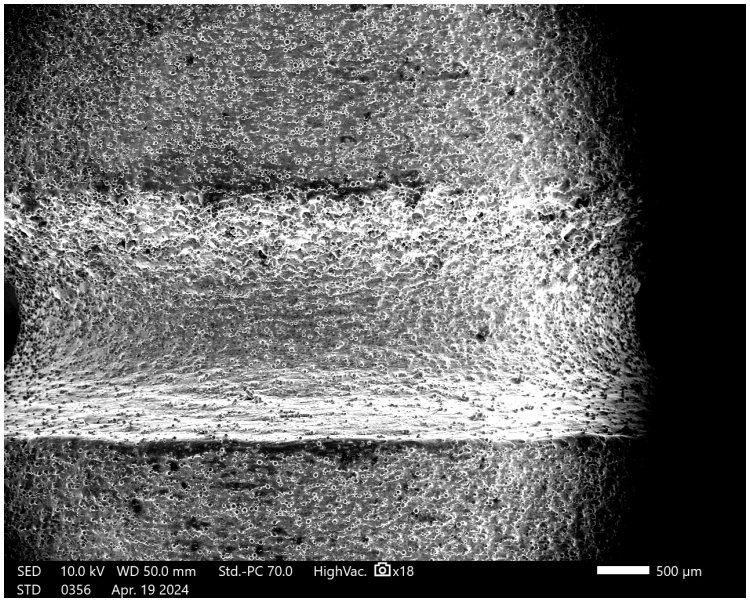

Figure 56: A2.30.5 Specimen

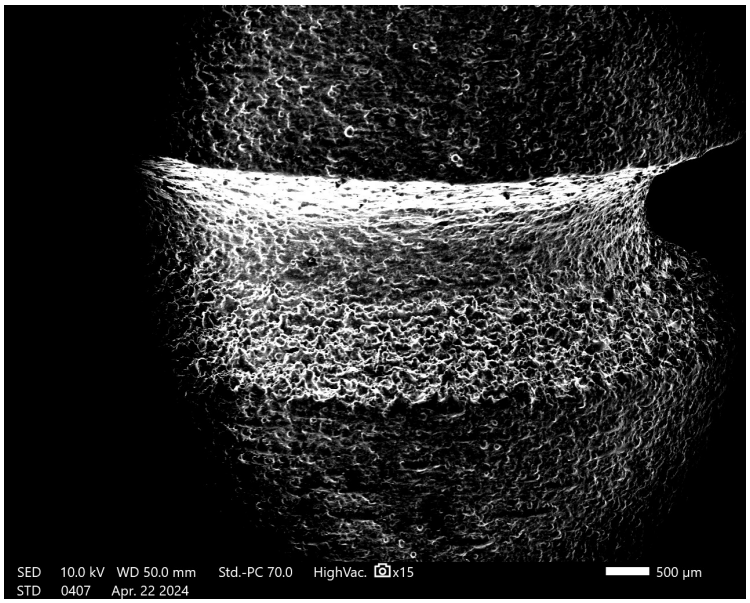

Figure 57: A2.30.6 Specimen

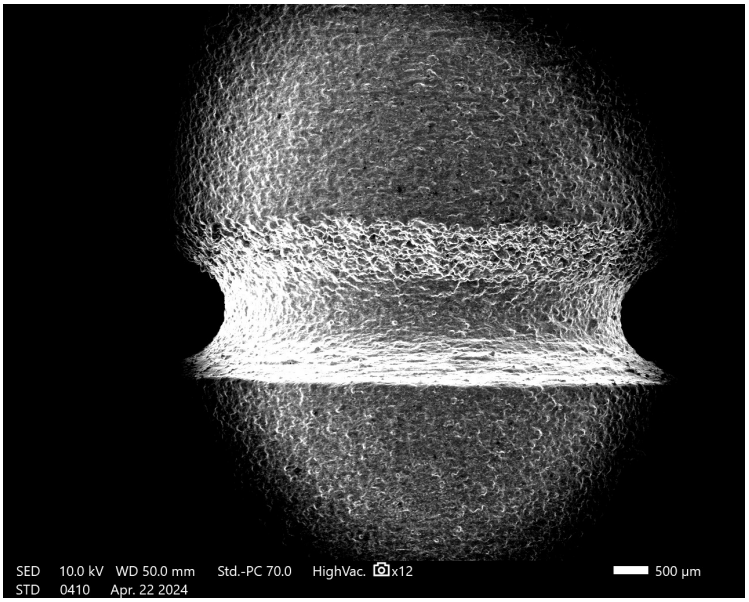

Figure 58: A2.30.7 Specimen

A.4 Notches pictures of A3 specimens

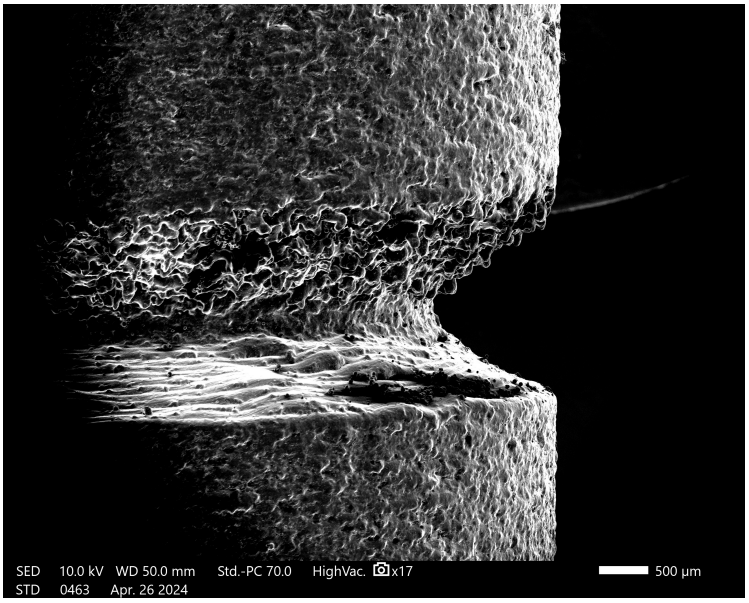

Figure 59: A3.2 Specimen

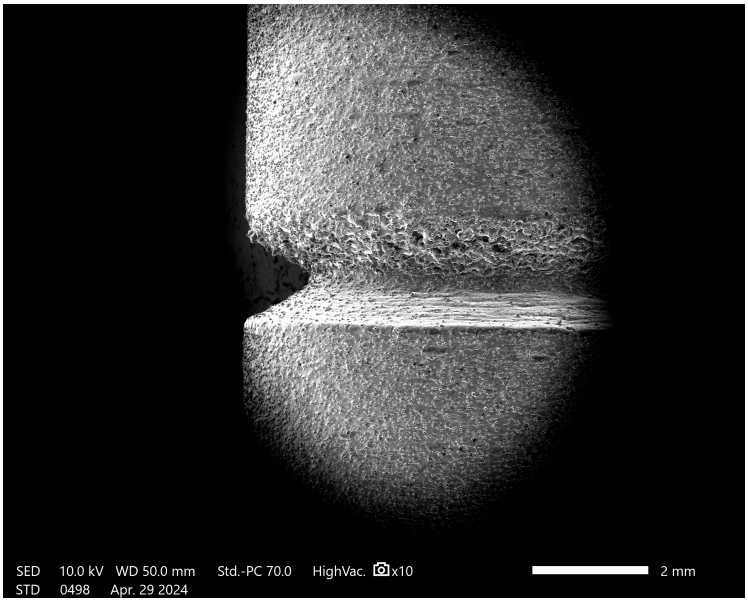

Figure 60: A3.6 Specimen

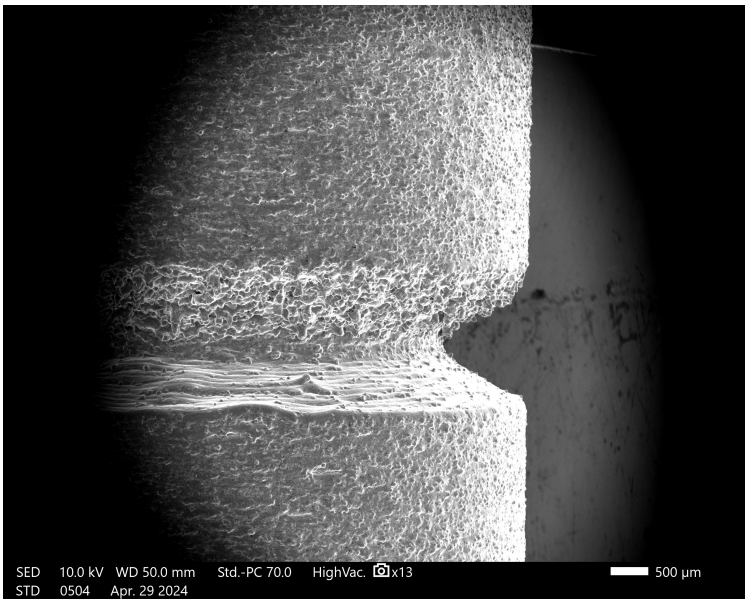

Figure 61: A3.7 Specimen

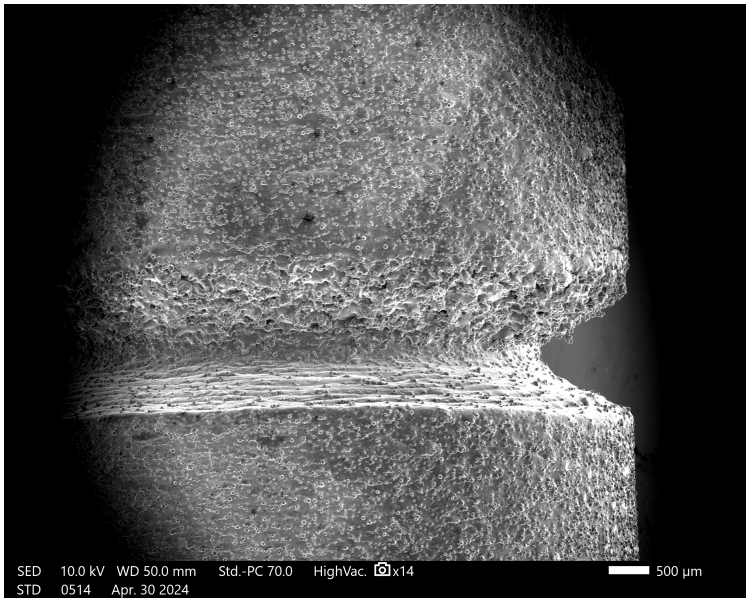

Figure 62: A3.9 Specimen

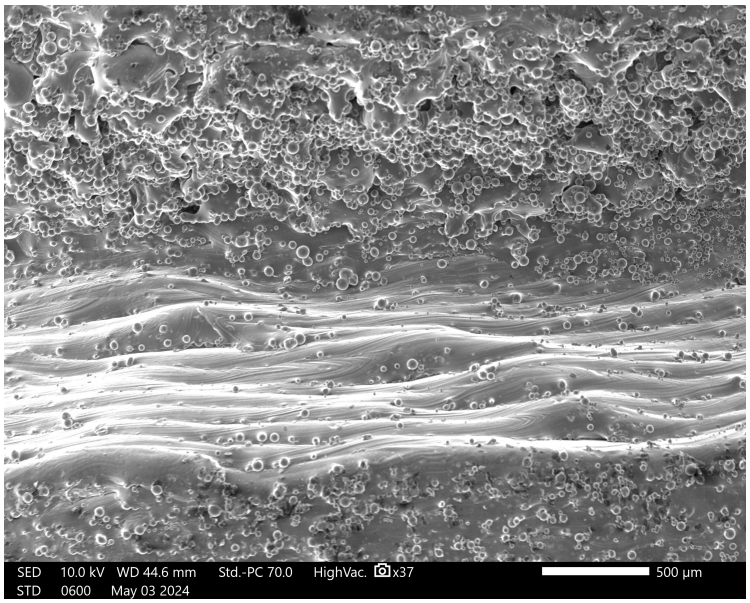

Figure 63: A3.12 Specimen

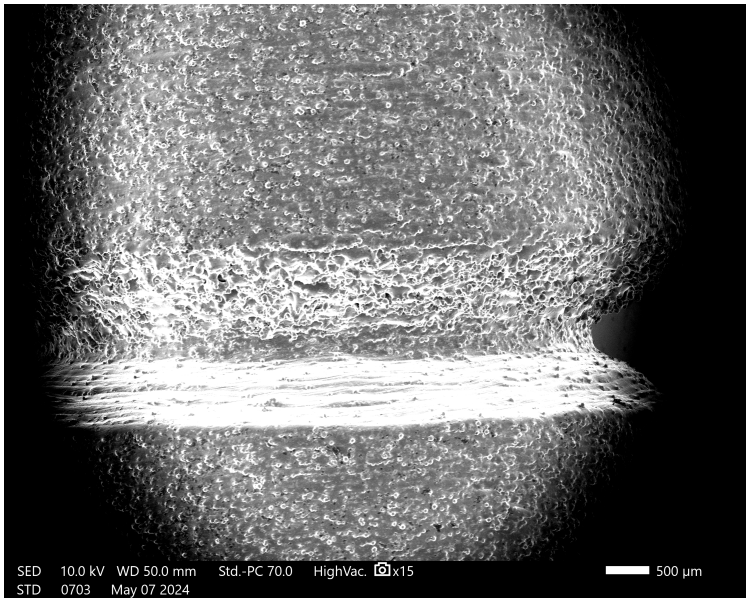

Figure 64: A3.15 Specimen

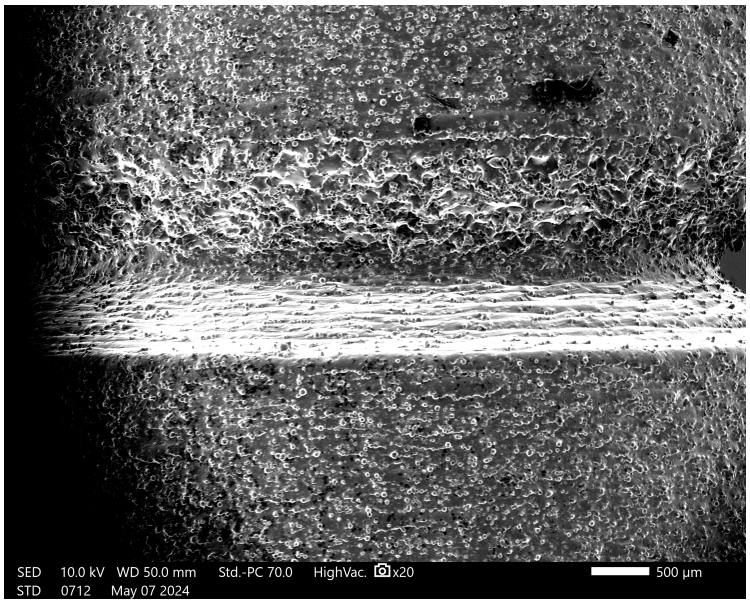

Figure 65: A3.17 Specimen

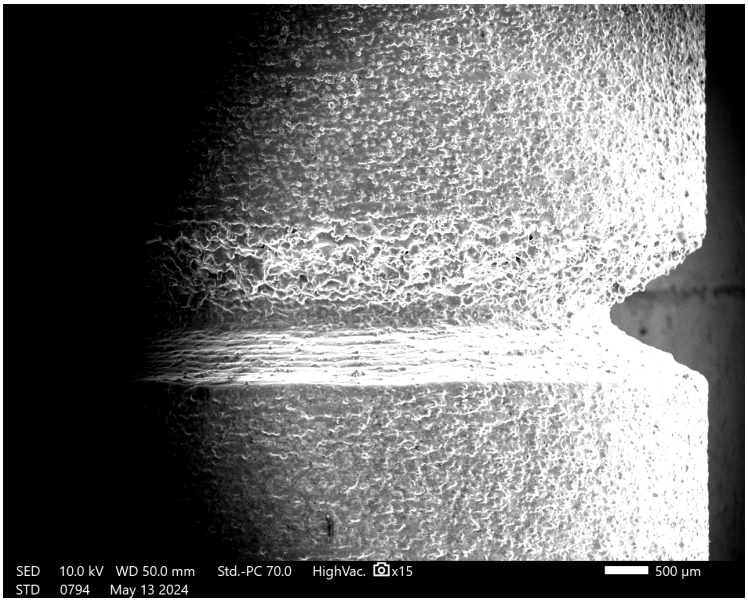

Figure 66: A3.23 Specimen

A.5 Fracture surfaces of hirtisation specimens

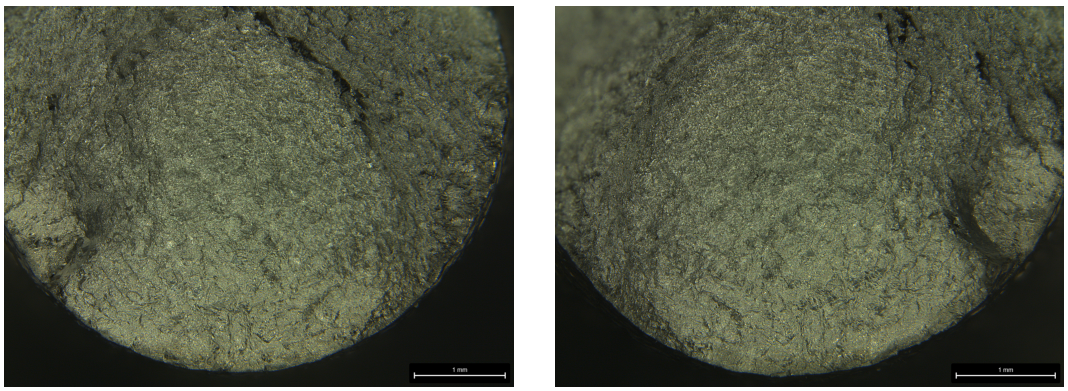

Figure 67: Fracture surface specimen H1.1.

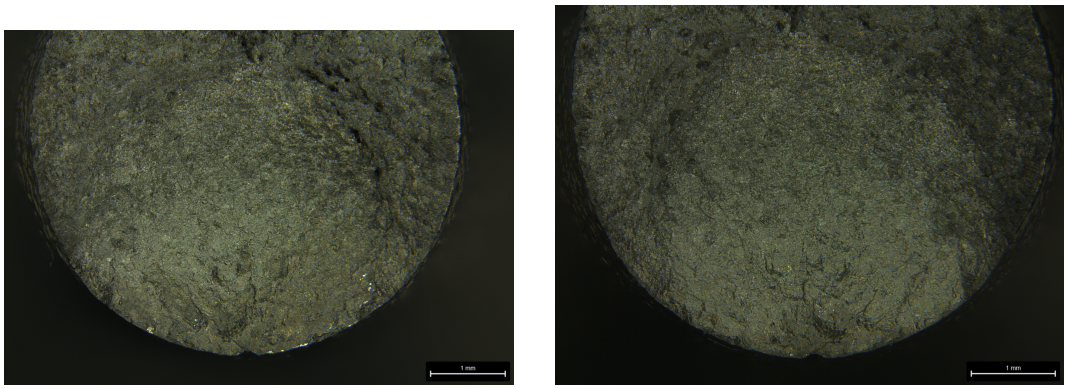

Figure 68: Fracture surface specimen H1.

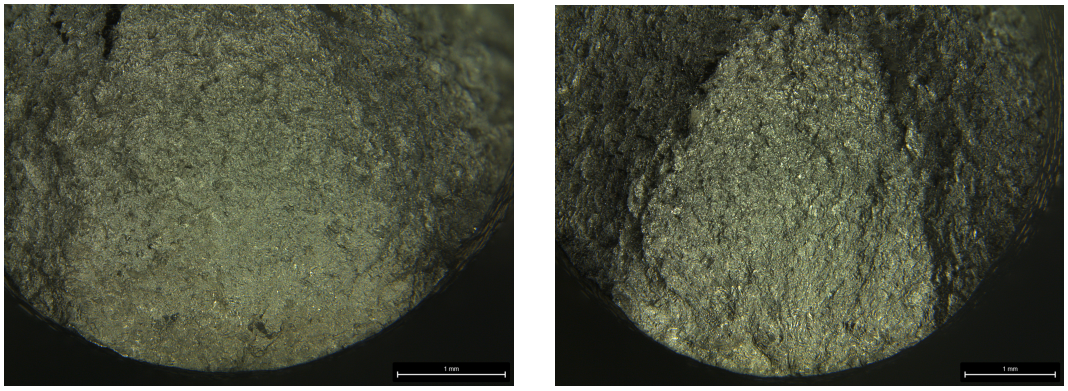

Figure 69: Fracture surface specimen H2.1.

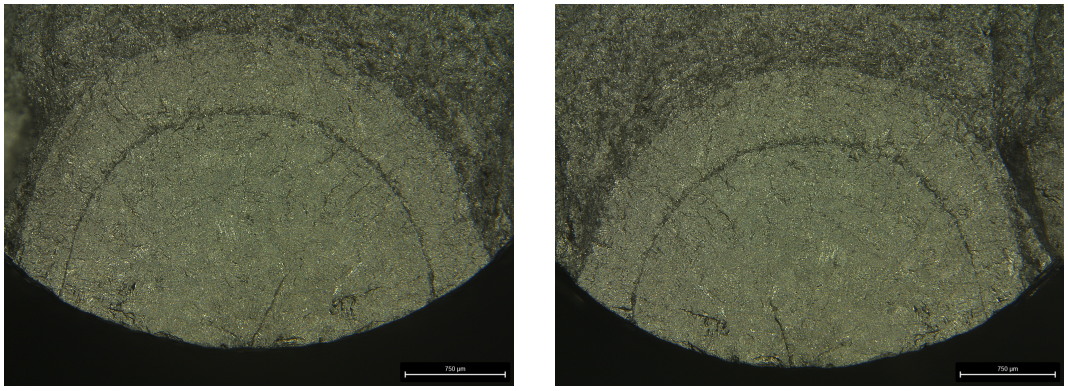

Figure 70: Fracture surface specimen H3.

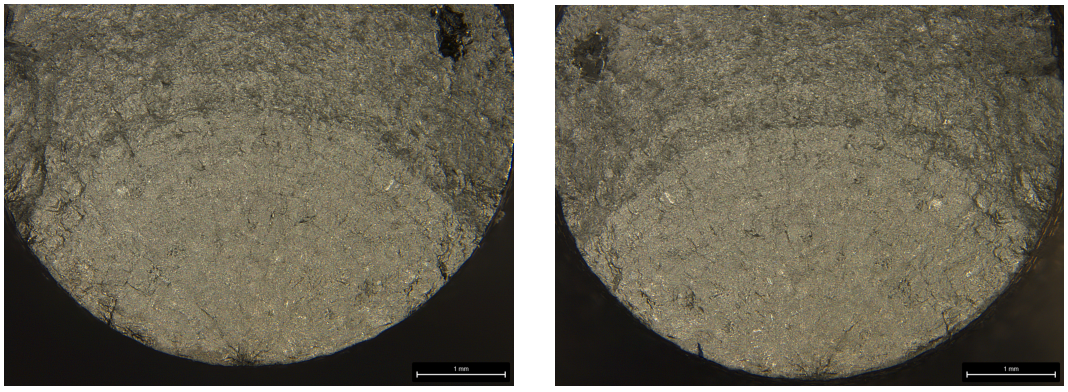

Figure 71: Fracture surface specimen H4.

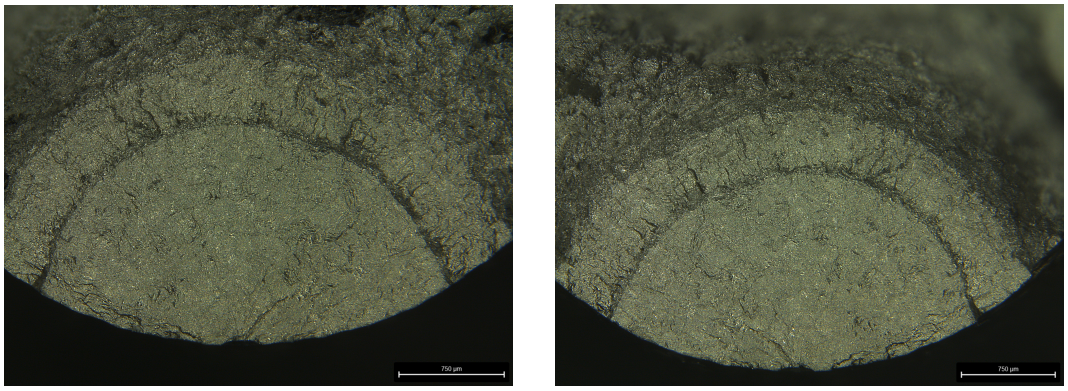

Figure 72: Fracture surface specimen H7.

A.6 Fracture surfaces of A2 specimens

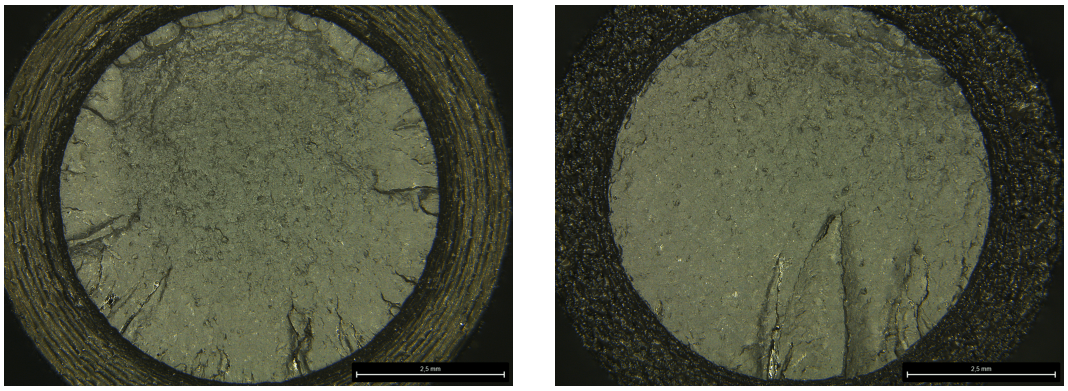

Figure 73: Fracture surface specimen A2.2:2 (left) A2.2:3 (right).

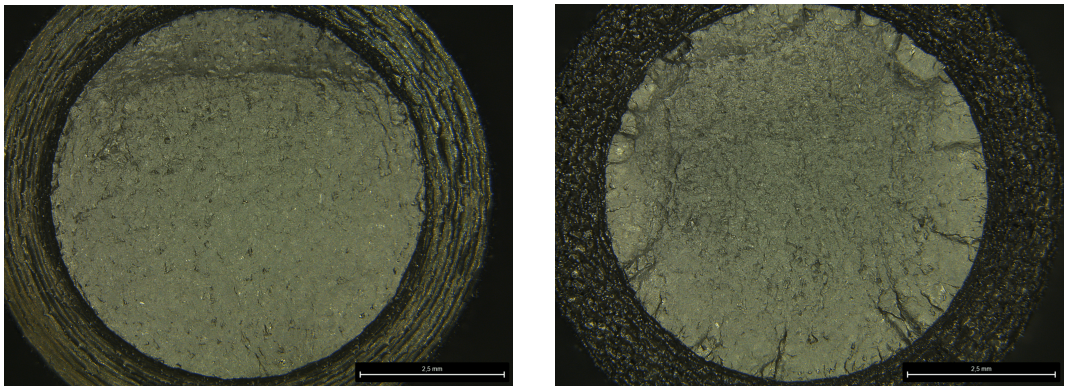

Figure 74: Fracture surface specimen A2.2:4 (left) A2.2:5 (right).

A.7 Fracture surfaces of A2.2 (30) specimens

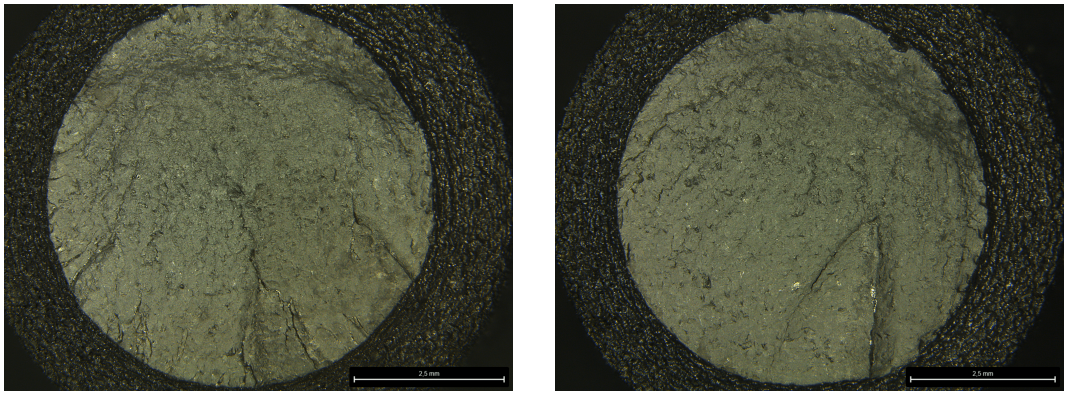

Figure 75: Fracture surface specimen A2.2(30):1 (left) A2.2(30):2 (right).

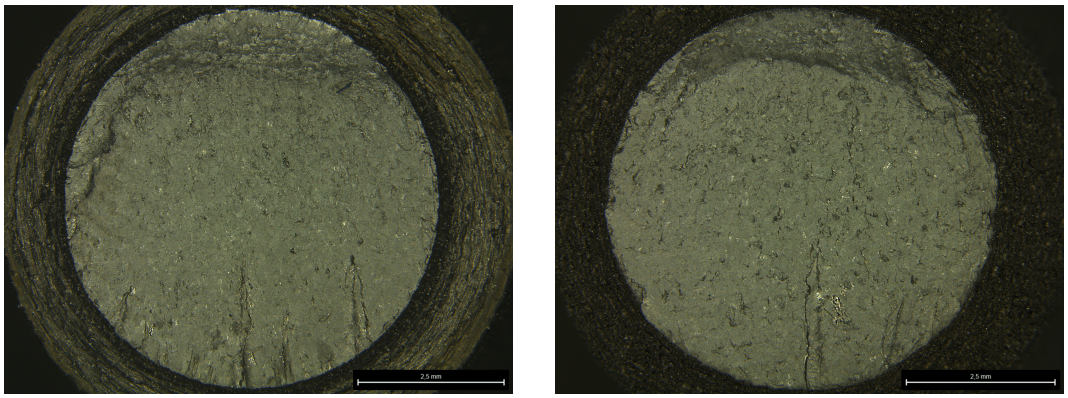

Figure 76: Fracture surface specimen A2.2(30):3 (left) A2.2(30):5 (right).

References

[1] Su A, Al'Aref SJ. History of 3D printing. In: 3D printing applications in cardiovascular medicine. Elsevier; 2018. p. 1-10.

[2] Najmon J, Raeisi S, Tovar A. In: Review of additive manufacturing technologies and applications in the aerospace industry; 2019. .

[3] Weflen ED. A hybrid additive and subtractive manufacturing approach for multi-material components; 2020. Available from: `https://api.semanticscholar.org/CorpusID:221379370`.

[4] Froes FH, Boyer R. Additive manufacturing for the aerospace industry. Elsevier; 2019.

[5] Najmon J, Raeisi S, Tovar A. In: Review of additive manufacturing technologies and applications in the aerospace industry; 2019. .

[6] Frazier W. Metal Additive Manufacturing: A Review. Journal of Materials Engineering and Performance. 2014 06;23.

[7] Fan H, Wang C, Tian Y, Zhou K, Yang S. Laser powder bed fusion (L-PBF) of Ti–6Al–4V/Ti–6Al–2Sn–4Zr–2Mo and Ti–6Al–4V/γ-TiAl bimetals: Processability, interface and mechanical properties. Materials Science and Engineering: A. 2023;871:144907.

[8] Fan H, Wang C, Tian Y, Zhou K, Yang S. Laser powder bed fusion (L-PBF) of Ti–6Al–4V/Ti–6Al–2Sn–4Zr–2Mo and Ti–6Al–4V/γ-TiAl bimetals: Processability, interface and mechanical properties. Materials Science and Engineering: A. 2023;871:144907.

[9] Hajare DM, Gajbhiye TS. Additive manufacturing (3D printing): Recent progress on advancement of materials and challenges. Materials Today: Proceedings. 2022;58:736-43.

[10] Eckel ZC, Zhou C, Martin JH, Jacobsen AJ, Carter WB, Schaedler TA. Additive manufacturing of polymer-derived ceramics. Science. 2016;351(6268):58-62.

[11] Spowart JE, Gupta N, Lehmhus D. Additive manufacturing of composites and complex materials. Jom. 2018;70:272-4.

[12] Herzog D, Seyda V, Wycisk E, Emmelmann C. Additive manufacturing of metals. Acta Materialia. 2016;117:371-92.

[13] Nguyen HD, Pramanik A, Basak A, Dong Y, Prakash C, Debnath S, et al. A critical review on additive manufacturing of Ti-6Al-4V alloy: Microstructure and mechanical properties. Journal of Materials Research and Technology. 2022;18:4641-61.

[14] Molaei R, Fatemi A, Sanaei N, Pegues J, Shamsaei N, Shao S, et al. Fatigue of additive manufactured Ti-6Al-4V, Part II: The relationship between microstructure, material cyclic properties, and component performance. International Journal of Fatigue. 2020;132:105363.

[15] Durant A. Additive Manufacturing Takes Flight. 2014;9:34-7.

[16] Najmon JC, Raeisi S, Tovar A. Review of additive manufacturing technologies and applications in the aerospace industry. Additive manufacturing for the aerospace industry. 2019:7-31.

[17] Froes F, Boyer R, Dutta B, Hills A. ADDITIVE MANUFACTURING FOR AEROSPACE APPLICATIONS–Part II: Fabrication of aerospace components using additive manufacturing has matured to the point where part microstructures and mechanical properties compare well with those of conventionally produced material. Advanced Materials & Processes. 2017;175(6):18-23.

[18] Singamneni S, Yifan L, Hewitt A, Chalk R, Thomas W, Jordison D. Additive manufacturing for the aircraft industry: a review. J Aeronaut Aerosp Eng. 2019;8(1):351-71.

[19] Plocher J, Panesar A. Review on design and structural optimisation in additive manufacturing: Towards next-generation lightweight structures. Materials & Design. 2019;183:108164.

[20] Joshi SC, Sheikh AA. 3D printing in aerospace and its long-term sustainability. Virtual and physical prototyping. 2015;10(4):175-85.

[21] Francois MM, Sun A, King WE, Henson NJ, Tourret D, Bronkhorst CA, et al. Modeling of additive manufacturing processes for metals: Challenges and opportunities. Current Opinion in Solid State and Materials Science. 2017;21(4):198-206.

[22] Nguyen HD, Pramanik A, Basak A, Dong Y, Prakash C, Debnath S, et al. A critical review on additive manufacturing of Ti-6Al-4V alloy: Microstructure and mechanical properties. Journal of Materials Research and Technology. 2022;18:4641-61.

[23] Kahlin M. 3D printing for Aerospace: Fatigue Behaviour of Additively Manufactured Titanium. PhD. 2021;Linkoping University Electronic Press.

[24] Kahlin M, Ansell H, Moverare JJ. Fatigue behaviour of additive manufactured Ti6Al4V, with as-built surfaces, exposed to variable amplitude loading. International Journal of Fatigue. 2017 Oct;103:353-62. Available from: https://www.sciencedirect.com/science/article/pii/S0142112317302736.

[25] Kahlin M, Ansell H, Moverare J. Fatigue crack growth for through and part-through cracks in additively manufactured Ti6Al4V. International Journal of Fatigue. 2022;155:106608.

[26] Direct R. Surface Roughness Chart: Understanding Surface Finish in Manufacturing. Rapid Direct; 2021. https://www.rapiddirect.com/blog/surface-roughness-chart/.

[27] ISO. ISO 4287-1997, Geometrical product specifications. ISO; 1997. https://www.iso.org/standard/72226.html.

[28] Ardi D, Li Y, Chan K, Blunt L, Bache M. Surface topography and the impact on fatigue performance. Surface Topography: Metrology and Properties. 2015 03;3:015007.

[29] Lu D, Liu Z, Wei X, Chen C, Wang D. Effect of post-processing methods on the surface quality of Ti6Al4V fabricated by laser powder bed fusion. Frontiers in Materials. 2023;10:1126749.

[30] Oosterbeek RN, Sirbu G, Hansal S, Nai K, Jeffers JR. Effect of hirtisation on the roughness and fatigue performance of porous titanium lattice structures. arXiv preprint arXiv:230406621. 2023.

[31] Beevers E, Neumayer D, Bonvoisin B, Brandão A, Hansal S, Doppler M, et al. Effect of Hirtisation treatment on surface quality and mechanical properties of AlSi10Mg samples produced by laser powder bed fusion. Materials Today Communications. 2024;38:108042.

[32] Ingrassia T, Nigrelli V, Ricotta V, Tartamella C. Process parameters influence in additive manufacturing. In: Advances on Mechanics, Design Engineering and Manufacturing: Proceedings of the International Joint Conference on Mechanics, Design Engineering & Advanced Manufacturing (JCM 2016), 14-16 September, 2016, Catania, Italy. Springer; 2017. p. 261-70.

[33] Miller KJ. THE BEHAVIOUR OF SHORT FATIGUE CRACKS AND THEIR INITIATION PART II-A GENERAL SUMMARY. Fatigue and Fracture of Engineering Materials and Structures. 1987;10.

[34] Siemens. S-N curve, Fatigue. Siemens Community; 2019. https://community.sw.siemens.com/s/article/what-is-a-sn-curve.

[35] Pilkey WD. Peterson's Stress Concentration Factors. 2nd ed. John Wiley and Sons, Inc; 1997.

[36] LBF I NLR. FALSTAFF: Description of a fighter aircraft loading standard for fatigue evaluation.. Joint publication of Flugzeugwerke Emmen, Switzerland; Laboratorium fur Betriebsfestigkeit (LBF), Germany; National Aerospace Laboratory (NLR), Netherlands; and Industrie-Anlagen-Betriebsgesellschaft mbH (IABG) G.; 1976.

[37] CEAT. CEAT Report M7681900. Centre d'Essais Aeronautique de Toulouse; 1980.

[38] Hashin Z, Rotem A. A cumulative damage theory of fatigue failure. Materials Science and Engineering. 1978;34.

[39] Instron. Materials Testing Machines for Tensile, fatigue, impact.; 2024. https://www.instron.com/.

[40] Leica-Microsystems. M125 C and M205 C Encoded stereo microscopes; 2024. https://www.leica-microsystems.com/.

[41] Jaturunruangsri S. Evaluation of material surface profiling methods: contact versus non-contact. Brunel University London; 2015. http://bura.brunel.ac.uk/handle/2438/10431.

[42] Mitutoyo. Mitutoyo SJ-410 series; 2024. https://www.mitutoyo.com/.

[43] Fashanu FF, Marcellin-Little DJ, Linke BS. Review of surface finishing of additively manufactured metal implants. In: International manufacturing science and engineering conference. vol. 84256. American Society of Mechanical Engineers; 2020. p. V001T03A013.

[44] Bologna O, Cecchel S, Cornacchia G, Avanzini A, Sepe R, Berto F, et al. Investigating post-processing impact on fatigue performance in LPBF Ti6Al4V with heat treatment, high pressure heat treatment, and dry electropolishing strategies. International Journal of Fatigue. 2024:108365.

[45] Lu D, Liu Z, Wei X, Chen C, Wang D. Effect of post-processing methods on the surface quality of Ti6Al4V fabricated by laser powder bed fusion. Frontiers in Materials. 2023;10:1126749.

[46] Maleki E, Bagherifard S, Unal O, Revuru M, Bandini M, Guagliano M. The efficiency of tumble finishing as a final post-treatment for fatigue enhancement of notched laser powder bed fusion AlSi10Mg. Scientific Reports. 2023;13(1):4602.

[47] Kahlin M. AMPeRE Vinnova funded Research and Development project. Vinnova.

[48] Balamurugan. Data-driven approaches for fatigue prediction of Ti–6Al–4V parts fabricated by laser powder bed fusion. International Journal of Fatigue. 2024 May;182.

[49] Schnabel K, Baumgartner J, Möller B. Fatigue assessment of additively manufactured metallic structures using local approaches based on finite-element simulations. Procedia Structural Integrity. 2019;19:442-51.